iScience

CellPress
OPEN ACCESS

Article

Pancreatic cancer organoid-screening captures personalized sensitivity and chemoresistance suppression upon cytochrome P450 3A5-targeted inhibition

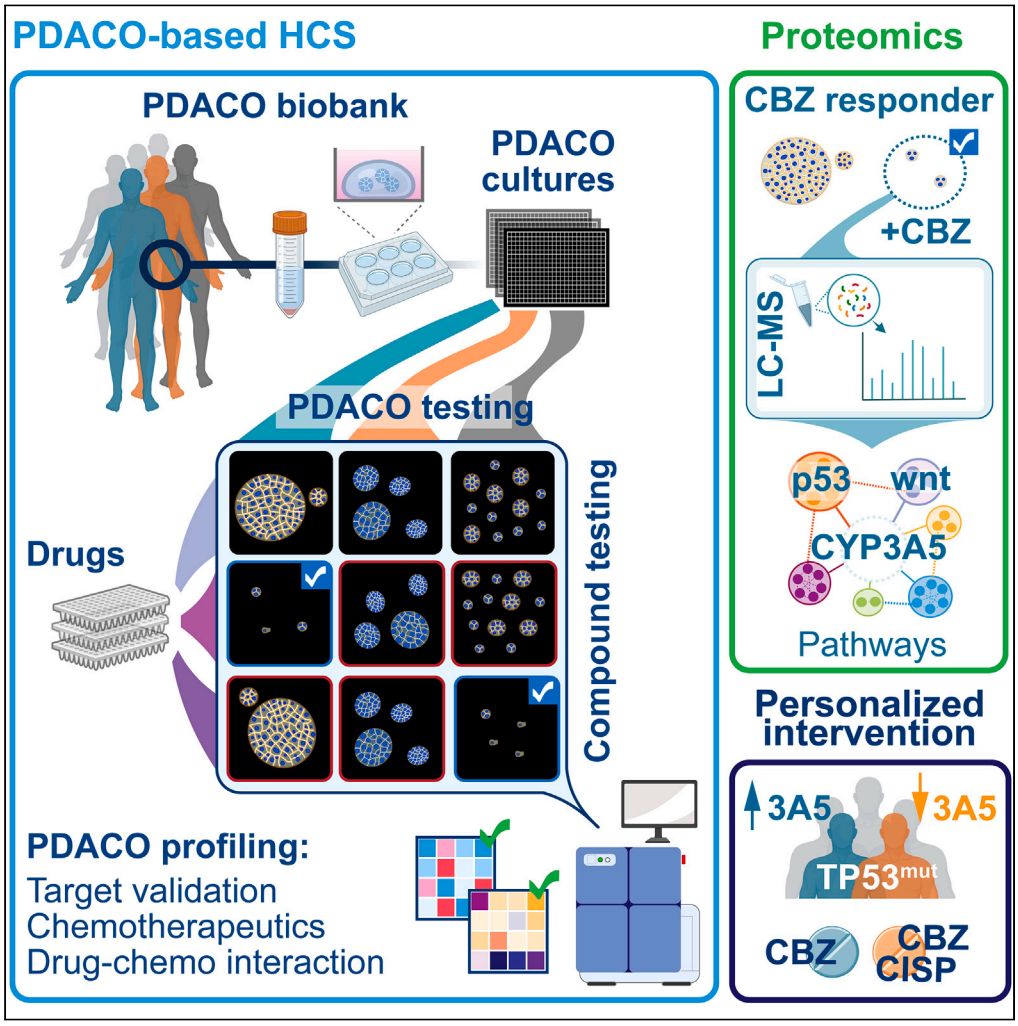

Meritxell B. Cutrona, Jing Wu, Ka Yang, Junmin Peng, Taosheng Chen

meritxell.baocutrona@stjude.org (M.B.C.)
taosheng.chen@stjude.org (T.C.)

Highlights

HCI-based screen on PDACO enables the scoring of drug repurposing and targets

Inhibiting CYP3A5 by CBZ sensitizes PDACO with medium-high levels of CYP3A5

Limiting the active pool of CYP3A5 enables personalized anti-cancer therapy

Inhibition of CYP3A5 suppresses p53 pro-oncogenic mechanisms in PDACO

Cutrona et al., iScience 27, 110289
July 19, 2024
https://doi.org/10.1016/j.isci.2024.110289

iScience

CellPress
OPEN ACCESS

Article

Pancreatic cancer organoid-screening captures personalized sensitivity and chemoresistance suppression upon cytochrome P450 3A5-targeted inhibition

Meritxell B. Cutrona,[1,4,*] Jing Wu,[1] Ka Yang,[2] Junmin Peng,[2,3] and Taosheng Chen[1,4,*]

SUMMARY

Cytochrome P450 3A5 (CYP3A5) has been proposed as a predictor of therapy response in subtypes of pancreatic ductal adenocarcinoma cancer (PDAC). To validate CYP3A5 as a therapeutic target, we developed a high-content image organoid-based screen to quantify the phenotypic responses to the selective inhibition of CYP3A5 enzymatic activity by clobetasol propionate (CBZ), using a cohort of PDAC-derived organoids (PDACOs). The chemoresistance of PDACOs to a panel of standard-of-care drugs, alone or in combination with CBZ, was investigated. PDACO pharmaco-profiling revealed CBZ to have anti-cancer activity that was dependent on the CYP3A5 level. In addition, CBZ restored chemo-vulnerability to cisplatin in a subset of PDACOs. A correlative proteomic analysis established that CBZ caused the suppression of multiple cancer pathways sustained by or associated with a mutant form of p53. Limiting the active pool of CYP3A5 enables targeted and personalized therapy to suppress pro-oncogenic mechanisms that fuel chemoresistance in some PDAC tumors.

INTRODUCTION

Pancreatic ductal adenocarcinoma (PDAC), the most prevalent and aggressive malignancy of the pancreas, is expected to become the second deadliest cancer in less than two decades.[1] PDAC is characterized by a dismal prognosis fueled by the high incidence and rapid acquisition of resistance to cytotoxic chemotherapy.[2,3] The persistent treatment failure calls for intensifying drug-discovery programs.[4] However, high-throughput screening (HTS) campaigns conducted in two-dimensional (2D) PDAC cultures have been demonstrated to be inefficacious,[5,6] indicating that cellular models better suited to recapitulating disease phenotypes *in vitro* may be more appropriate for screening drugs.[7] The use of advanced cellular models of cancer, such as tumor organoids,[8–10] has started to redirect HTS toward precision and personalized medicine.[11–16] PDAC-derived organoids or PDACOs,[17] which are established from adult stem cells obtained from biopsies and surgically resected tumors,[18–20] retain key phenotypic aspects and functional features of the parental tumor.[4,16,21,22] Head-to-head comparisons of the drug response in PDACO models vs. patient clinical outcomes have shown a close correlation between the two,[4,23,24] highlighting the translational power of these models in preclinical testing setups.

The stratification of patient-derived tumor organoids according to molecular signatures[4,21,25] has proved useful for assessing chemotherapy regimens on a per-patient basis and for nominating alternative treatment options. A member of the cytochrome P450 family 3A (CYP3A), CYP3A5, is highly expressed in exocrine-like PDACs,[26] which correlates with the high expression rates reported in PDAC cellular models.[27] This heme-containing mono-oxygenase is involved in metabolizing xenobiotic substances such as chemotherapeutics.[28] Accordingly, it was proposed that enhanced CYP3A5 expression caused the inactivation of CYP3A5-metabolized drugs within tumor cells, engaging a mechanism for cancer cell–autonomous clearance of drugs and resistance thereto.[26] Consequently, limiting CYP3A5 activity in cancer cells may alleviate chemoresistance to at least a subset of therapeutics.

To explore the possibility of targeting CYP3A5 in PDAC, a selective inhibitor of CYP3A5 is needed. Recently, our laboratory identified clobetasol propionate (CBZ) as an enzymatic inhibitor that selectively binds and targets CYP3A5.[27,29] Although, CBZ is an FDA-approved antimycotic drug,[30] and has been utilized in drug repurposing studies directed at evaluating remyelination in the context of multiple sclerosis,[31] the therapeutical potential of CBZ as anti-PDAC drug has not been explored yet. In the present study, we established a PDACO-driven high-content screening (HCS) platform to interrogate and dissect the therapeutic benefit of the chemical inhibition of CYP3A5 by using high-content imaging (HCI). Here, we show that CYP3A5 is druggable in *ex vivo* tumor models derived from patients and that high levels of CYP3A5 protein correspond to CBZ vulnerability in a subset of PDACOs. As patient-derived organoid platforms are of high interest for the development of drug-repurposing strategies to identify previously unknown vulnerabilities that will enable *de novo* therapy-induced organoid killing

[1]Department of Chemical Biology and Therapeutics, St. Jude Children's Research Hospital, Memphis, TN 38105-3678, USA
[2]Department of Structural Biology, St. Jude Children's Research Hospital, Memphis, TN 38105-3678, USA
[3]Department of Developmental Neurobiology, St. Jude Children's Research Hospital, Memphis, TN 38105-3678, USA
[4]Lead Contact
*Correspondence: meritxell.baocutrona@stjude.org (M.B.C.), taosheng.chen@stjude.org (T.C.)
https://doi.org/10.1016/j.isci.2024.110289

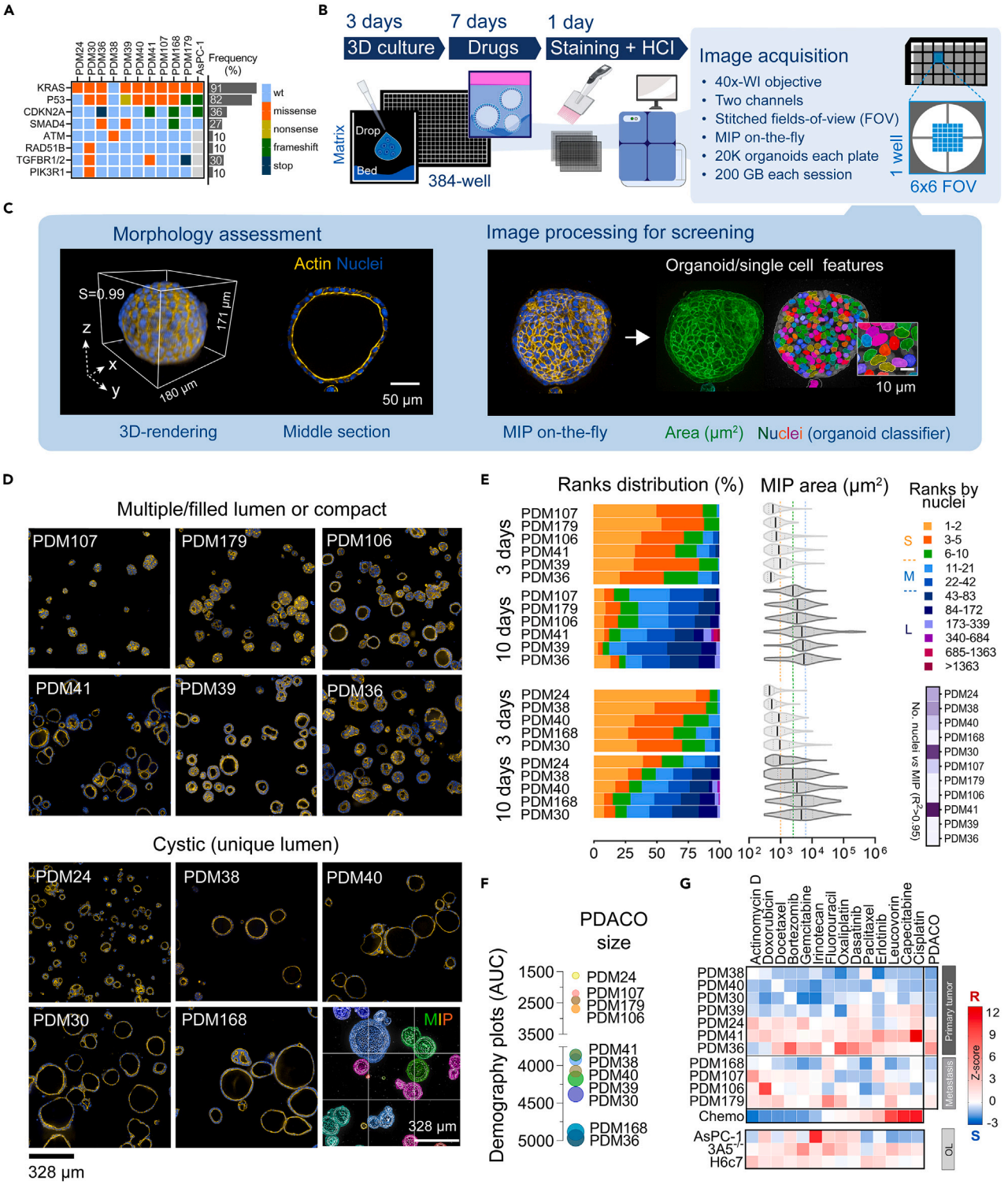

Figure 1. HCI-based morpho-profiling and pharmaco-profiling of PDACOs

(A) Oncoplot of our cohort of PDACO and OL models. The full list of mutations can be found in Table S1.

(B) Schematic indicating the PDACO-HCS workflow for 3D growth, drug treatment, fixation, staining, automated confocal imaging, and extraction of morpho-phenotypes from individual organoids formed in 96-well or 384-well plates. An HCI regimen was selected to ensure a cost-effective capture of organoid information in the heterogeneous cohort of PDACOs utilizing a 40× water immersion (WI) objective.

Figure 1. *Continued*

(C) The images illustrate the preserved 3D spherical architecture of organoids after fixation. On-the-fly MIP images supported the segmentation of details from individual organoids and cells. Scale bars are 50 μm and 10 μm (inset).

(D) Confocal images from nine fields of view (FOVs) stitched together to display PDACO morpho-phenotypes across our cohort. The collection comprises lines of organoids bearing a unique central lumen (e.g., cystic morphology) and lines with filled or multiple lumina, solid or absent lumina, or a mixture of the different architectures. Actin is stained yellow, nuclei are stained blue. An example of a segmentation mask of organoid MIPs applied to nine FOVs is included. PDM, patient-derived model. Scale bars are 328 μm. More detail on PDACO-specific architectural features can be observed in Figure S1.

(E) Stacked bar chart showing the percentage of organoids for each organoid size rank in each population of PDACOs in the unperturbed condition. Frequency profiles at 3 and 10 days of culture are shown. The profiles feature the abundance of each organoid size rank, defined by the number of nuclei detected in every organoid MIP (small, <11 nuclei; medium, <43 nuclei; large, ≥43 nuclei; see Figure S1A). The definition of ranks is based on a fixed term of arbitrary cell division (e.g., 24 h). Violin plots show organoid sizes in PDACO cultures over time, based on the average area of the organoid MIPs (in μm^2) extracted from individual organoids. The violin plots display the MIP sizes as the median and quartiles, using a $\log_{10}$ scale. The heatmap depicts the linear regression analysis of the area and the number of nuclei of MIPs. R-squared values greater than 0.95 are indicated (violet). Most of the cystic PDACOs fitted into the regression model. N_{ORG} = 4399 (at 3 days old), N_{ORG} = 3605 (at 10 days old); data are pooled from quadruplicate wells in a 96-well plate.

(F) Classification of PDACOs as small, medium, or large based on demography plots extracted from the frequency profiles and calculation of the area under the curve (AUC), see Figure S1B. The AUC values were used as demography scores. N_{ORG} = 4963 (dataset from three independent experiments after 10 days of 3D growth).

(G) Heatmap visualization of PDACO therapy response, including models derived from primary tumors (PTs) or metastatic sites (PMs) and implemented with organoid-like cultures (OLs). Values are row z-scored changes in MIP for each drug, calculated from normalization to DMSO for the respective PDACOs. Cumulative effects of individual chemotherapeutics (chemo) and PDACOs are included. Resistance scores (positive, R, in red) and sensitivity scores (negative, S, in blue) are indicated. MIP size was determined by batch image analysis. The screening plates included well replicates for DMSO and positive controls. $N_{ORG/OL}$ = 8579.

by drug combination,[32] we sought to test whether the inhibition of CYP3A5 could overcome chemoresistance to some drugs using our HCS approach. By applying a drug combinatorial screen for a list of standard-of-care chemotherapeutics and using CBZ as an anchor, we uncovered an effective, actionable sensitivity to cisplatin. A correlative proteomics analysis revealed that the PDACO response to CBZ occurs via the blockade of cancer cell maintenance pathways and points to functional crosstalk, at least with the G105R mutant version of p53. Our study unlocks the potential of personalized treatment for PDAC by targeting CYP3A5 via CBZ.

RESULTS

High-content screening captures inter-patient and intra-patient pancreatic ductal adenocarcinoma cancer-derived organoids heterogeneity in the unperturbed state

To enable HCI screening in PDACOs, we established a protocol for miniaturizing extracellular matrix (ECM)-embedded cultures of pancreatic cancer organoids[19] by adapting a pipeline previously validated in a colon carcinoma spheroid model.[33] We assessed the morphology of 11 primary PDACO lines[34] derived from primary tumors or from metastatic sites and carrying different oncogenic mutations (Figure 1A and Table S1). Our all-in-one approach (Figure 1B) was ideated to support the quantitative image-based profiling of patient-derived models (PDMs) in the steady state or after perturbation by drugs. To extract morphometric information from the entire population of organoids generated in each well, two features were used as a proxy for organoid size: the area of the maximum intensity projection (MIP) of the organoids and the demographic stratification of the population in categories based on the organoid size as ranked by the number of nuclei within the MIP (Figure 1C, S1A and S1B).

Organoid cultures in ECM exhibited substantial intra-PDACO heterogeneity with respect to individual organoid sizes (Figure 1D). Therefore, we assessed whether our organoid readouts supported inter-PDACO comparisons. We analyzed the demographic profiles of the organoid size categories at the population level (Figure 1E). After 3 days in culture, there was a clear over-representation of small organoids or clusters of a few cells in all PDACO sets. At 10 days, the representation of organoids with medium or large numbers of nuclei within the MIP increased within each PDACO population (Figure 1E). These data indicated that all lines retained their proliferative state in our three-dimensional (3D) culture multi-well plate assay. The 10-day PDACO lines were rank-ordered by size from small to large by integrating the demographic data (Figure 1F and S1B), which corresponded well with the average MIP areas for each PDACO population (Figure 1E; violin plots), as verified across independent experiments (Figure S1C). Morphological differences of PDACOs in the unperturbed state were observed by the visualization of higher magnification images (Figures S1D, S1E, and S1F), suggesting PDACO-specific signature architectural features at the organoid level. Our HCI-based survey of PDACO sizes confirmed that there was considerable size heterogeneity at the inter-PDACO and intra-PDACO levels and validated our morphometric readouts for inter-patient comparisons of PDACOs in the unperturbed state.

Patient-specific responses to chemotherapeutics in pancreatic ductal adenocarcinoma cancer-derived organoids and organoid-like models

We used the MIP area as the primary measurement for assessing PDACO responses to drug perturbations and for establishing organoid growth vulnerabilities. To test the sensitivity of our HCI assay, we selected a list of FDA-approved drugs used in chemotherapy (neoadjuvant, adjuvant, or targeted) of PDAC (Table S2) or other gastrointestinal cancers. To exclude general drug toxicity effects and to score the

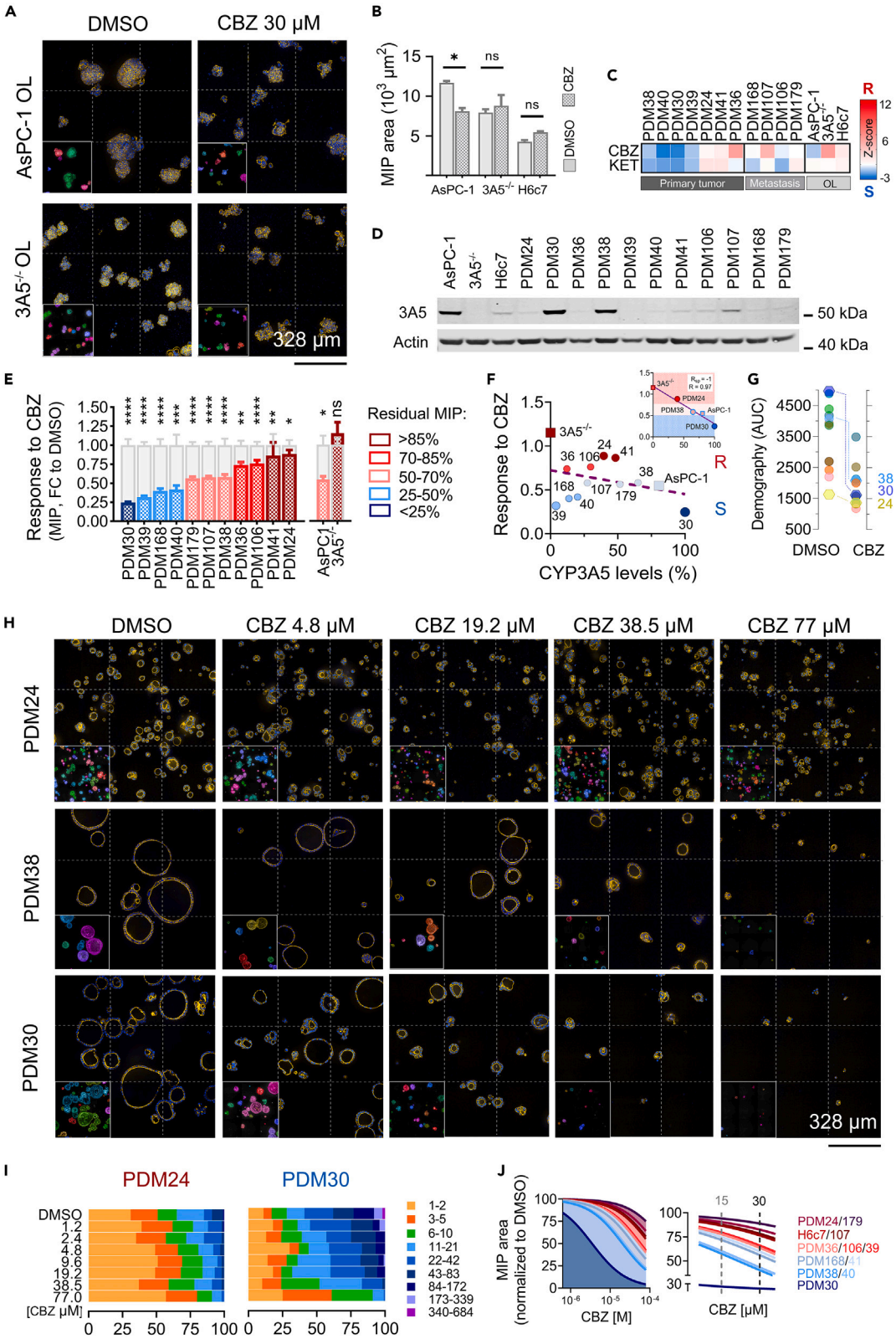
A
DMSO
CBZ 30 μM
AsPC-1 OL
3A5-/- OL
328 μm
B
MIP area (10^3 μm^2)
15
10
5
*
ns
ns
CBZ
DMSO
AsPC-1
3A5-/-
H6c7
C
PDM38
PDM40
PDM30
PDM39
PDM24
PDM41
PDM36
PDM168
PDM107
PDM106
PDM179
AsPC-1
3A5-/-
H6c7
CBZ
KET
Primary tumor
Metastasis
OL
Z-score
R
S
12
6
-3
D
AsPC-1
3A5-/-
H6c7
PDM24
PDM30
PDM36
PDM38
PDM39
PDM40
PDM41
PDM106
PDM107
PDM168
PDM179
3A5
Actin
50 kDa
40 kDa
E
Response to CBZ
(MIP, FC to DMSO)
1.50
1.25
1.00
0.75
0.50
0.25
0.00
PDM30
PDM39
PDM168
PDM40
PDM179
PDM107
PDM38
PDM36
PDM106
PDM41
PDM24
AsPC1
3A5-/-
Residual MIP:
>85%
70-85%
50-70%
25-50%
<25%
F
Response to CBZ
CYP3A5 levels (%)
3A5-/-
24
36
106
41
38
AsPC-1
168
107
179
40
39
30
R
S
G
Demography (AUC)
4500
3500
2500
1500
500
DMSO
CBZ
38
30
24
H
DMSO
CBZ 4.8 μM
CBZ 19.2 μM
CBZ 38.5 μM
CBZ 77 μM
PDM24
PDM38
PDM30
328 μm
I
PDM24
PDM30
DMSO
1.2
2.4
4.8
9.6
19.2
38.5
77.0
[CBZ μM]
0
25
50
75
100
1-2
3-5
6-10
11-21
22-42
43-83
84-172
173-339
340-684
J
MIP area
(normalized to DMSO)
100
75
50
25
0
10-6
10-5
10-4
CBZ [M]
15
30
CBZ [μM]
PDM24/179
H6c7/107
PDM36/106/39
PDM168/41
PDM38/40
PDM30

Figure 2. Suppression of 3D growth via CBZ responds to CYP3A5 expression in a PDACO-dependent and dose-dependent manner

(A and B) Visualization and quantitative characterization of the response to 30 μM CBZ in AsPC-1, 3A5$^{-/-}$, and H6c7 OLs (see Figure S2). Representative images of nine FOVs showing response to CBZ in parental AsPC-1 OLs. Scale bar: 328 μm. Data in the bar chart show organoid MIP size as the mean ± SEM of measurements in triplicate from 96-well plates. *$p < 0.02$; n.s., not significant by ordinary one-way ANOVA with Tukey's multiple comparisons test. Total N_{OL} = 446.

(C) Row z-scored changes in average MIP area with CBZ or KET normalized to DMSO treatment from primary screening show PDACO-specific responses to the selective inhibition of CYP3A5 or pan-inhibition of CYP3A. MIP size was determined by batch image analysis. $N_{ORG\cdot DMSO}$ = 1359; $N_{ORG\cdot CBZ}$ = 1774; $N_{ORG\cdot KET}$ = 2323.

(D) Immunoblot showing the basal levels of CYP3A5 in PDACOs and OLs. Immunoblots indicating CYP3A5 induction after exposure to CBZ are included in Figure S3.

(E) Quantitative characterization of the CBZ response in PDACOs and OLs across independent experiments. The measurements were extracted from an independent validation experiment (with quadruplicate wells) and pooled with organoid data from the primary screening obtained by supervised segmentation. N_{ORG} = 10743. The histograms report the average fold change in organoid MIP area (mean ± SEM) after treatment with 30 μM CBZ. DMSO control bars for each line are shown in gray to illustrate the organoid shrinkage that occurred in lines treated with CBZ (bars in color). Quantitative classification of the organoid shrinkage response by tiers of residual MIP defines sensitivity as major (≤25% residual MIP), minor (up to 50%), or mild (≤70%), as compared with resistant or non-responder organoids (≥70% residual MIP). ****$p < 0.0001$, ***$p < 0.001$ **$p < 0.01$, *$p < 0.05$; *n.s.*, not significant (by Mann–Whitney test).

(F) Scatterplot of z-scores for organoid responses to CBZ of PDACO and OLs compared to normalized levels of CYP3A5 protein at the basal level as quantified by immunoblot analysis. Protein levels were normalized to PDM30 to enable comparison across the set. R-squared of regression analysis (R) = 0.1 ($p < 0.28$). The inset shows the same analysis for the PDM24/38/30 subset and OL controls. Spearman correlation (R_{sp}) = −1 ($p < 0.02$) and R-squared of regression analysis (R) = 0.97 ($p < 0.002$). Resistance scores (R, in red) and sensitivity scores (S, in blue) are indicated. See Figures S4A and S4B for comparison.

(G) AUC scores extracted from datasets pooled together (Figure 2E), depict the response to CBZ for collectives of organoids. All PDACO lines responded. The effect on the PDM24/38/30 subset shows proportionality with the levels of CYP3A5 protein, with PDM24 displaying 16% modification relative to the original population structure, followed by 49% in PDM38 and 67% in PDM30.

(H) Representative confocal images of nine FOVs illustrating the pharmaco-typing of CBZ in PDM24 (a hyposensitive PDACO with low levels of CYP3A5), as compared with PDM30 (a hypersensitive PDACO with the highest levels of CYP3A5) or PDM38 which also displayed sensitivity to CBZ in a dose-response manner. Insets show individual segmented organoids in pseudo-color. Scale bar: 328 μm.

(I) Demography profiles tracking the major responsiveness of PDM30 to CBZ across increasing dosages of this compound. PDM30 demography profile shows statistical significance ($p < 0.0001$ by Chi-square test of equal frequences).

(J) Dose–response (DR) analysis for CBZ and full PDACO cohort (Figure S4A), using FC values on organoid MIPs plotted as the mean ± SEM from three technical replicates in 96-well plates. N_{ORG} = 11524. Fitting curves and CBZ IC_{50} were calculated with MIPs normalized to DMSO and across the CBZ DR range. The rightmost panel displays a segment of the fitting curves comprised between 15 μM and 30 μM CBZ dosages for the stratification of the PDACO with respect to their response to CBZ.

responsiveness of the organoids, we grew the normal duct epithelial cell line H6c7[35] as organoid-like cultures (hereafter referred as to OLs). Likewise, we included parental AsPC-1[36] cells and two CYP3A5 knockout (KO) (3A5$^{-/-}$) cell lines[27] grown as OLs (Figures S2A and S2B). The overall aim was to represent a well-characterized PDAC cell line that expressed high levels of CYP3A5 and its KO counterparts as respective reporters of the opposing potential contributions of CYP3A5 to chemoresistance.

All PDACOs and OLs were grown for 3 days in 384-well plates and treated with the panel of drugs at a single concentration for 7 days (Figure 1B and Table S2). The *in vitro* therapy response (Figure 1G) revealed patient-specific patterns of sensitivity to individual drugs. Such profiles displayed no correspondence with the original tumor type (e.g., primary tumor [PT] vs. primary metastasis [PM]) or organoid size (Spearman's R = −0.13; see in Figure S4), suggesting the involvement of molecular determinants. Quantitative cumulative scores showed that approximately 60% of the drugs tested failed to elicit a sensitive response in organoids. Erlotinib, leucovorin, capecitabin, and cisplatin ranked as the top chemoresistance agents. Similarly, 45% of the PDACOs, such as the PT PDACOs PDM24/41/36 and the PM PDACOs PDM106/179, displayed major resistance to treatments. The H6c7 OLs did not respond to chemotherapeutics. The 3A5$^{-/-}$ OLs showed higher rates of insensitivity when compared with the AsPC-1 OLs (Figure 1G), suggesting that ablating CYP3A5 protected the cells from the action of the chemotherapeutics. Our results highlight the fidelity of our PDACO-HCS workflow in capturing inter-patient heterogeneous responses to drugs in primary organoid and OL models, enabling rapid pharmaco-profiling and confirming that drug sensitivity can vary on a per-patient basis.

Clobetasol propionate inhibits pancreatic ductal adenocarcinoma cancer-derived organoids growth in a cytochrome P450 3A5 level–dependent and patient-specific manner

We took advantage of the genetic ablation of CYP3A5 in the AsPC-1 cellular background to assess whether the biological effects of chemical inhibition by CBZ could be ascribed specifically to the loss of function of CYP3A5. The AsPC-1 OLs showed 3D growth vulnerability to CBZ, whereas the 3A5$^{-/-}$ OLs displayed no significant response (Figure 2A and 2B), thereby implicating CYP3A5 expression in the shrinkage response of the AsPC-1 OLs. Compared to the parental AsPC-1 OLs, the 3A5$^{-/-}$ OLs displayed a basal 3D growth defect that was not detectable in classical spheroid cultures (Figures S2A and S2B). CBZ inhibition of CYP3A5 in the AsPC-1 OLs caused shrinkage similar to that evoked by the genetic ablation of 3A5$^{-/-}$ (Figure 2B), reinforcing the perception that the effects of CBZ were mediated specifically by CYP3A5 as a consequence of its selective chemical inhibition. In addition, we compared the effects of CBZ on AsPC-1 2D cultures vs. the OL and found that the response to CBZ in parental AsPC-1 was undetectable in 2D culture (Figure S2C), in line with a previous study.[27] Like the 3A5$^{-/-}$ OLs, the H6c7 OLs remained insensitive to CBZ (Figure 2B) as validated by CBZ dose-response analysis (Figure S2D).

We harnessed our PDACO-based screening approach to profile the effects of the selective inhibition of CYP3A5 via CBZ in primary PDAC models. For a direct comparison with the pan-inhibition of CYP3A isoforms, ketoconazole (KET)[37] treatment was also included. Patterns of patient-specific but also non-overlapping responses to CBZ and KET were detected (Figure 2C). To assess whether CBZ vulnerability correlated with CYP3A5 levels, we performed Western blot analysis of protein levels in the set of PDACOs in the steady state (Figure 2D). Within the subset of cystic PTs, PDM24, PDM38, and PDM30 expressed lower, equal, and higher levels of CYP3A5, respectively, when compared with the AsPC-1 OLs. The other PDACO lines expressed modest or very low levels of CYP3A5. Profiling CBZ effects across independent measurements revealed PDACO-specific degrees of susceptibility to a single dosage of CBZ (30 μM; Figure 2E). The PDACOs were classified as high responders (e.g., PDM30), medium-to-low responders (e.g., PDM39/168/40/179/107/38), or non-responders (e.g., PDM106/36/41/24) based on the residual MIP detected after treatment (Figure 2E). We observed a low association between CYP3A5 levels and the PDACO response to CBZ when we considered the whole cohort ($R = 0.1$, $p = 0.28$; Figure 2F). However, we identified a subset of PDACO (i.e., PDM24/38/30; Figure 2F, inset) that showed an excellent fit ($R = 0.97$, $p < 0.002$; Spearman's $R = -1$, $p < 0.02$), which was compatible with the shifts on demography scores observed (Figure 2G). Our data indicated that medium-to-high levels of CYP3A5 might predispose the PDACOs to CBZ susceptibility, but the response to CBZ for low CYP3A5 expressers is less predictable. Finally, CBZ exposure increased the CYP3A5 levels in all PTs (Figure S3A), probably reflecting a response to xenobiotic exposure.[26] The PDM24/38/30 subset displayed good proportionality of increased expression on top of the initial basal levels. Importantly, this upregulation failed in the $3A5^{-/-}$ and H6c7 OLs (Figure S3B), suggesting that PDACOs are prone to respond to CBZ only when CYP3A5 is consistently produced and there is an ongoing malignancy status. Overall, our findings underline the fact that CBZ does not act through a generic cytotoxic effect but in a CYP3A5 level-dependent manner.

Organoid shrinkage shows clobetasol propionate dose dependency in pancreatic ductal adenocarcinoma cancer-derived organoids with high cytochrome P450 3A5 levels

Given that CYP3A5 expression levels, and consequently the extent of inhibition by CBZ, dictated the suppression of organoid growth in a subset of PDACOs, we next evaluated whether this effect occurred in a dose-responsive manner. We applied sequential dilutions of CBZ for 7 days to all PDACO lines (Figure S4A) and examined the morphological response of PDM24/38/30 in detail, as these lines represented, respectively, hypo-, moderate- and hyper-responders to CBZ, with full correspondence in the degree of organoid shrinkage and levels of CYP3A5 (Figure 2E and 2F). Upon examining the morphologies of PDM24 populations across increasing CBZ concentrations, we observed minimal changes in organoid MIP size (Figure 2H) and shifts in the organoid size distribution with CBZ concentrations below 77 μM (Figure 2I and S3C). In contrast to the results with PDM24, treating PDM30 with increasing CBZ dosages resulted in marked and progressive shrinkage of the organoids (Figure 2H), as confirmed by the rapid decline in the medium and large size categories at the population level, which was appreciable at dosages below 10 μM (Figure 2I and S3C). Such decrements did not reflect any deviation of the MIP size from the originally assigned rank (Figure S3D). Like PDM30, in PDM38 organoids we also observed a progressive shrinkage to increasing concentrations of CBZ, although more attenuated upon receiving a similar dose (Figure 2H). The dose–response (DR) analysis of average organoid MIP size across the range of CBZ concentrations evidenced dose dependency for CBZ in PDM30 and PDM38, as compared with PDM24 (Figure 2J and Figure S4A). A similar trend was observed in AsPC-1 parental and $3A5^{-/-}$ OL counterparts (Figure S2D). We calculated the CBZ IC_{50} value for each PDACO and classified the lines in correspondence to their dynamic range of CBZ inhibition (Figure S4A). Such classification confirmed the original stratification (e.g., 65% of coincidence) obtained by single-dose analysis of CBZ (Figure 2E). A regression analysis (Figure S4B) of AUC values from the CBZ DRCs in Figure S4A vs. CYP3A5 levels, confirmed that medium-high expressors of CYP3A5 such as PDM38 and PDM30, correlate with enhanced vulnerability to CBZ compared to CYP3A5 low expressers.

Therefore, our compound profiling confirmed CBZ to be a potent dose-dependent inhibitor of tumor organoid growth in those cases that presented high levels of CYP3A5 protein expression.

A chemo–clobetasol propionate combination screen reveals an intersection of clobetasol propionate with capecitabine and cisplatin modes of action

By multivariate analysis, the CYP3A5-dependent response to CBZ could not be associated to the original PDACO's size or shape attributes (Figure S4C; Spearman's $R = 0.182$, $p = 0.595$) as visualized and measured at the unperturbed state (Figure 1 and S1) but was partially associable with the chemosensitivity of PDACOs and OLs (Spearman's $R = 0.66$, $p < 0.01$) (Figure S5A), indicating a putative common layer of vulnerability to the action of CBZ and to the drugs themselves. As CBZ is a derivative of the canonical glucocorticoid receptor (GR) agonist prednisolone (PRED), we evaluated the effects of PRED exposure to determine whether GR pathway modulation contributed to the effect of CBZ. The patterns of organoid response to PRED, as obtained from the organoid MIP measures (Figures S5B and S5C), did not match those observed with CBZ (Figures S5and 2C). Specifically, PRED did not cause significant shrinkage in PDM24/38/30 organoids or in AsPC-1 and $3A5^{-/-}$ OLs (Figure S5D). Therefore, any association of GR agonism with the signatures of organoid size response to chemotherapeutics across the full panel of PDACOs (Spearman's $R = 0.2$, $p < 0.48$) could be excluded.

To detect any interaction between CBZ perturbation and the mode of action of the tested chemotherapeutics in an unbiased manner, we conducted a single-dose screen of the drug–CBZ combination, using CBZ as an anchor. By calculating the $\log_2$-transformed fractional inhibition ratio (FIR) of the average MIPs for co-treatment and treatment with the drug alone, we identified possible synergistic drug–CBZ combinations (Figure 3A). Up to 16 synergistic combinations out of 182 pairwise combinations were detected ($\log_2$[FIR] = <−1; 8.8% enrichment), suggesting that combining most chemotherapeutics with CBZ did not modify the response to the monotherapies. True synergistic combination hits were established after assessing the inhibitory responses and comparing the quantitative effects of drug–CBZ co-treatment

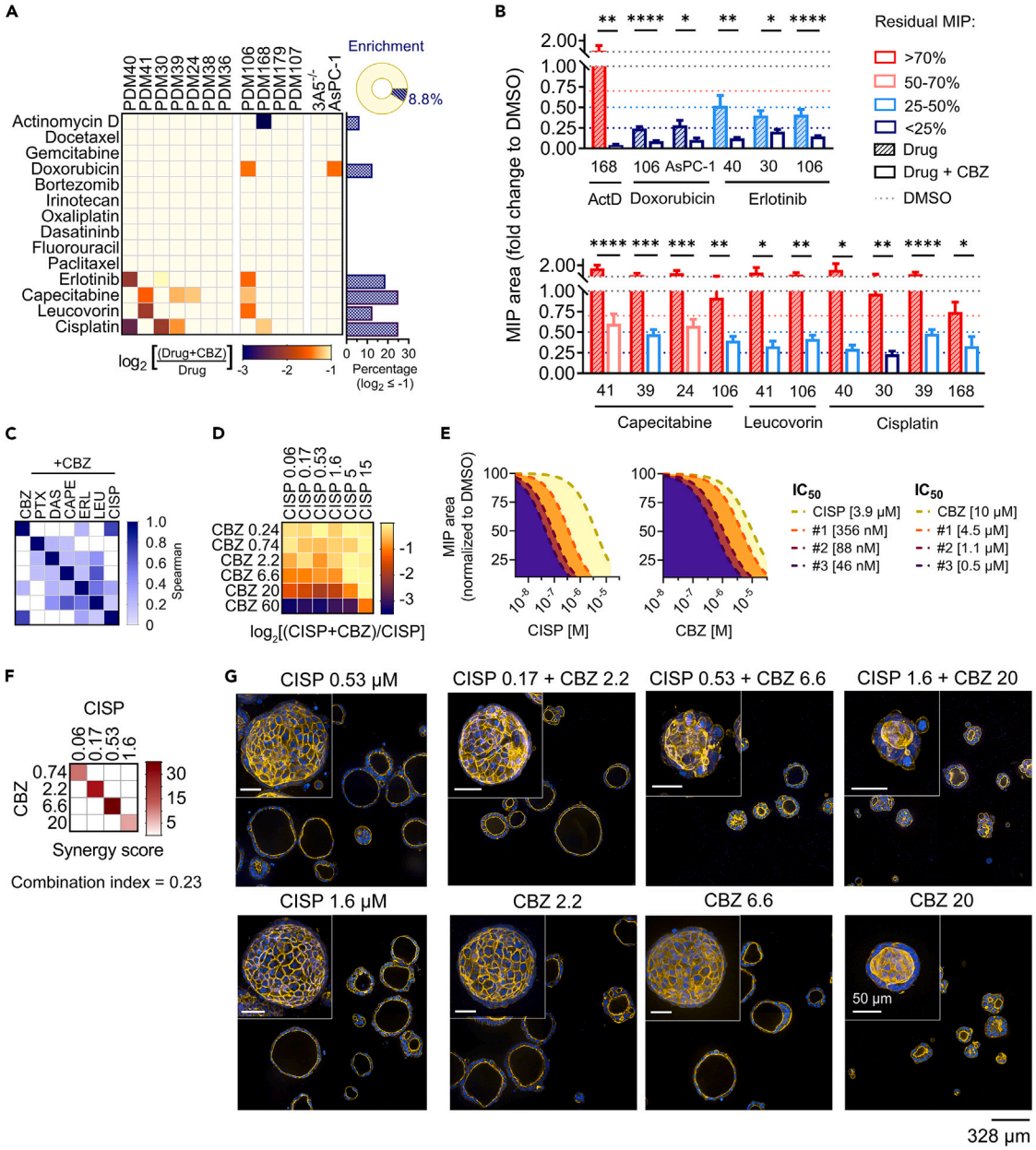

Figure 3. Detection and validation of synergism between CBZ and cisplatin

(A) Heatmap of the drug–drug interaction or combination response in PDACO and OL models after 7 days of co-treatment with the drug plus CBZ. Drugs were administered at the concentrations indicated in the primary screening. CBZ was applied at a dosage of 30 µM. The gradient from yellow to blue indicates aggravating pairs. The cut-off score was set at $\log_2$ [FIR] ≤ -1. The pie chart depicts the enrichment set of potential chemo–CBZ interacting pairs. The bars show the percentage of synergistic interactions for each drug within the enrichment set. All data were obtained after the supervised segmentation of individual organoid MIPs. For more details of the drug profiles and drug interaction profiles of erlotinib, leucovorin, capecitabine, and cisplatin across all PDACOs with or without CBZ co-treatment see Figure S5. N_{ORG} = 12624.

(B) Bar charts show the inhibition of organoid MIP size (mean ± SEM) for drugs alone or in combination with CBZ from the enrichment set. All values are relative to DMSO controls for the respective PDACOs. The colors of the bars indicate FC values (dark blue, 0.25; light blue, 0.5–0.7; red, 0.7), which represent the tiers of residual MIP; the fill pattern indicates the type of treatment (stripes, drug alone; solid bars, drug in combination with CBZ). ****$p < 0.0001$, ***$p < 0.001$ **$p < 0.01$, *$p < 0.05$; *n.s.*, not significant (by Mann–Whitney test). ActD, actinomycin D.

(C) Spearman correlation between organoid response to CBZ and FIR scores for a subset of drugs and across the full panel of PDACOs. Spearman's R = 0.73 ($p <$ 0.02) for CBZ vs. CISP. Abbreviations: PTX, paclitaxel; DAS, dasatinib; CAPE, capecitabine; ERLO, erlotinib; LEU, leucovorin; CISP, cisplatin.

(D) DR matrix for cisplatin–CBZ drug combinations in PDM30 organoids in 96-well plates. The heatmap displays the synergism scores, calculated as the $\log_2$-transformed FIR. $N_{ORG \cdot DMSO}$ = 164; $N_{ORG \cdot CISP}$ = 538; $N_{ORG \cdot CBZ\ DR}$ = 607; $N_{ORG \cdot DR\ matrix}$ = 2986.

Figure 3. *Continued*

(E) Dose–response fitting curves calculated for three sets of combinations (diagonals; Figure S5) in the matrix. The DR curves and the corresponding IC_{50} values reveal a progressive decrease in the concentration of cisplatin required to impair 3D growth of PDM30 with increasing dosages of CBZ.

(F) Heatmap showing the highest single agent (HSA) coefficients calculated for significant cisplatin–CBZ interaction pairs (e.g., with synergy scores higher than 30). The total synergy score of the DR matrix was 10.75; combination index was 0.23.

(G) Representative confocal images of PDM30 organoids from one DR cisplatin–CBZ diagonal set, showing the effectiveness of the lowest concentrations of cisplatin (e.g., 0.17–1.6 μM) and CBZ (e.g., 0.74–6.6 μM) at arresting 3D growth and eliciting organoid shrinkage in combination. Representative images for lowest concentrations of cisplatin and CBZ alone are included. Scale bars: 328 μm and 50 μm (insets).

to those of treatment with the drug alone (Figure 3B). Among the well-established substrates of CYP3A5,[26] only erlotinib was confirmed as a synergistic combination hit for a modest subset in the enrichment set. In this case, the aggravating phenotype manifested on top of initial sensitive responses to erlotinib alone (Figure 3B). Notably, we observed a substantial frequency of synergy for CBZ combined with capecitabine or cisplatin (Figure 3A and 3B). In both cases, the co-treatment eliminated the high rates of resistance to capecitabine or cisplatin alone. A deeper analysis of the dataset by supervised image segmentation of organoids for the erlotinib, leucovorin, capecitabin, and cisplatin treatment sets (Figure S5E) revealed that the number of synergistic combination hits was even higher in the cisplatin subset, which scaled up to 37% of combinations in the enrichment set. Of note, PDM30, the higher expressor of CYP3A5 in our PDACO cohort, displayed the most evident aggravating inhibitory response with cisplatin–CBZ, in marked contrast to PDM24 (Figure S5E). A multivariate analysis (Figure 3C) confirmed that there was some association between the organoid response signatures for CBZ and the FIR scores for cisplatin–CBZ co-treatment (Spearman's $R = 0.73$, $p < 0.02$) across the PDACO cohort. Erlotinib but not cisplatin is a substrate of CYP3A5, therefore, in our PDACO set, the chemical inhibition of the drug-metabolizing potential of CYP3A5 via CBZ did not facilitate the action of most chemotherapeutics, including direct substrates of CYP3A5.[26] As cisplatin is not metabolized by CYP enzymes, our data could indicate that downstream effects of CYP3A5 inhibition intersect with cisplatin-mediated processes of cytotoxicity. This observation probably means that additional molecular layers dictate vulnerability to CBZ or vice versa.

Clobetasol propionate restores chemo-vulnerability to cisplatin

To confirm the synergism of cisplatin–CBZ effects in PDM30, we constructed a DR matrix of pairwise drug combinations. We extracted the MIP sizes relative to a DMSO control (Figure S5F) and calculated the FIR for each cisplatin–CBZ pair in the matrix. Plotting this information as heatmaps enabled the detection of three sets of combinations (Figure 3D) that indicated significant effectiveness with cisplatin by decreasing its initial concentration in the presence of CBZ (e.g., by a factor of 10–100) (Figure 3E). The effect of the cisplatin–CBZ combination was synergistic (combination index, CI = 0.23; Figure 3F and S5G), with the strongest compromised viability occurring with pairs located at the center of the DR matrix (Figure 3F). Visual inspection of the wells within a representative synergistic combination subset showed that the lowest concentrations of cisplatin and CBZ in combination were more effective at impairing the 3D growth of organoids than were cisplatin or CBZ alone at a comparable concentration (Figure 3G and S5F). Thus, our dissection of cisplatin–CBZ synergism confirmed CBZ to be a functional synergistic partner of cisplatin in PDM30.

Proteomic analysis of clobetasol propionate effects in patient-derived model 30

To identify the cellular pathways that respond to the inhibition of CYP3A5, we conducted a TMT proteomic analysis[38,39] in PDM30 and PDM24, as they exhibited higher and lower vulnerability, respectively, to CBZ. Analysis of differentially expressed proteins (DEPs) in organoids exposed to 20 μM CBZ for 48 h revealed an increased magnitude of upregulated and downregulated proteins in PDM30, as compared to PDM24 (Figure 4A). These proteins included CYP3A5 and members of the CYP family involved in xenobiotic metabolism (Figures S6A and S6B). Functional annotation enrichment analysis (Figure S6C) showed that CBZ treatment for 48 h caused the downregulation of proteins involved in various metabolic and biosynthetic pathways, including the generation of precursor metabolites and energy. We also observed the downregulation of modules involved in chromatin modification, redox homeostasis, the response to oxidative stress, the extracellular matrix, organelle organization, and cellular differentiation, among others. Differentially upregulated proteins were detected in pathways implicated in the cell cycle and nuclear division, DNA damage checkpoints, the mitotic spindle or microtubule-based processes, protein ubiquitination, and the cellular response to stress or to radiation. We generated a signature of the most representative pathways inhibited or activated by CBZ in PDM30 (Figure 4B). In PDM24 organoids exposed to CBZ, we detected none of the signature upregulated pathways seen in PDM30. The cell metabolism pathways downregulated in PDM30 were downregulated to a lesser extent in PDM24. After treating PDM30 organoids with CBZ for 7 days, we confirmed that the downregulation of metabolic pathways had persisted. However, this longer CBZ exposure resulted in the eventual decline of DNA replication pathways as well (Figure 4C).

Chemical inhibition of cytochrome P450 3A5 triggers defects in $TP53^{G105R}$ stability and Wnt-dependent cancer cell maintenance in patient-derived model 30

Because PDM30 harbors a G105R missense mutation in p53 (hereafter referred as to $TP53^{G105R}$) (Table S1) and because many of the shifts observed in pathways in the CBZ-treated PDM30 proteome (Figure S6C) could be ascribed to various mechanisms for adaptative responses promoted by mutant p53 proteins,[40] we investigated the link between our list of DEPs and $TP53^{G105R}$ in PDM30. We identified a subnetwork (Figure S6D) that defined a set of p53 turnover regulatory processes (Figure 4D) that were potentially perturbed by the inhibition of CYP3A5.

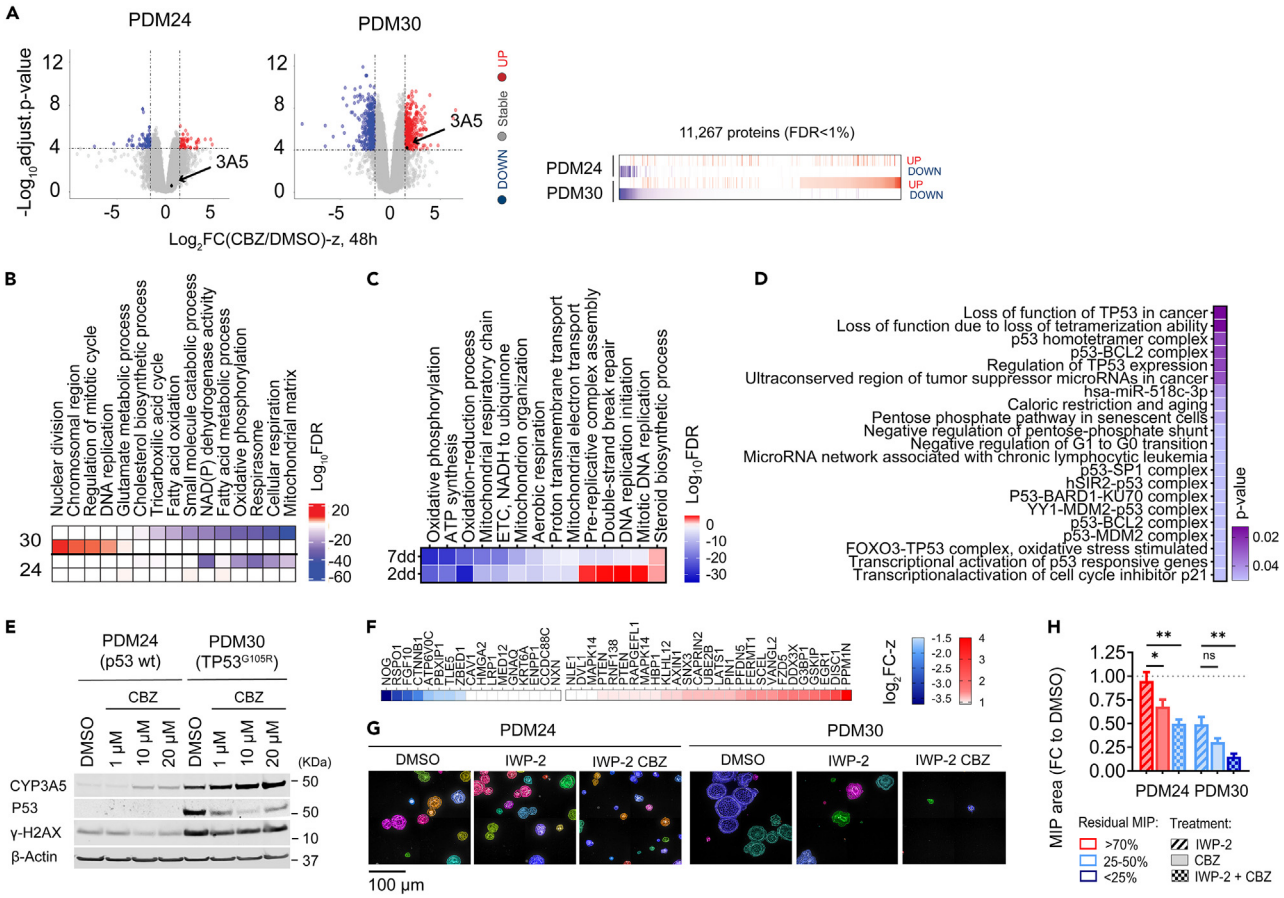

Figure 4. Proteome response to CYP3A5 inhibition via CBZ in PDM30 reveals defects in TP53^{G105R} stability and failure of Wnt signaling

(A) Volcano plots illustrating that some proteins are differentially abundant in PDM30 and PDM24 (see Figures S6A and S6B). The $\log_2$ fold changes ($\log_2$FC) were z-scaled, and cut-off criteria were set to $\log_2$ FC-z ≤ -2 or ≥ 2; FDR < 1%. More upregulated or downregulated proteins were detected in PDM30. DEP analysis was carried out by normalizing the results with CBZ to DMSO proteome sets extracted from organoids treated for 48 h. A set of 11,267 unique proteins with FDR <1% was extracted and analyzed. Blue denotes downregulation; gray, stable regulation; red, upregulation.

(B and C) Heatmap annotation of the significantly upregulated and downregulated functional modules in the PDM30 proteome. Log-transformed FDR values indicate the magnitude of the DE pathways shift relative to the same signature analyzed in PDM24 after 48 h of exposure to CBZ (B) or in the PDM30 proteome after 48 h or 7 days of CBZ treatment (C). Blue and red denote the FDR determined from downregulated and upregulated proteins, respectively.

(D) Predicted panel of enrichment for the most significant DEP-p53–connected pathways in PDM30 after treatment for 48 h with CBZ. $p < 0.05$. See also Figures S6C and S6D.

(E) Immunoblot analysis showing the total levels of p53 protein in PDM24 and PDM30, with histone γH2AX serving as a functional marker of response to DNA damage connected to p53 activity.

(F) DEP analysis of Wnt pathway components (GO:0016055) in PDM30 organoids treated with CBZ for 48 h. The heatmap lists candidate proteins whose abundance is modified by CBZ in PDM30. Blue, downregulation, $\log_2$FC-z ≤ -1.5; red, upregulation, $\log_2$FC-z ≥ 1.5; white, $\log_2$FC-z ≥ 1 or ≤ -1; FDR <1%. See also Figures S6E, S7 and S8.

(G and H) Effects of disrupting Wnt signaling with the porcupine inhibitor IWP-2 alone or in combination with CYP3A5 inhibition via CBZ in PDM24 and PDM30. Four representative FOVs are stitched together to show segmented organoids for each condition and PDACO (G). Scale bar: 100 µm. Bar charts show the residual organoid MIP size (mean ± SEM) for each treatment. All values are relative to DMSO controls (H). The colors of the bars indicate fold-change values (dark blue, 0.25; light blue, 0.5–0.7; red, 0.7), and the fill pattern indicates whether the organoids were treated with IWP-2 alone (stripes), CBZ alone (solid) or with IWP-2 in combination with CBZ (checks). $^{**}p < 0.01$; n.s., not significant (by Mann–Whitney test). N_{ORG} = 418.

TP53^{G105R} exhibits defects in conformation at the protein level[41] that mistarget its degradation through the ubiquitin–proteasome system. By Western blot analysis, we confirmed that treatment with CBZ for 7 days reduced the intracellular accumulation of TP53^{G105R} (Figure 4E), whereas, as expected, no changes were detected at the level of the wild-type p53 protein expressed in PDM24 (Figure 4E and Table S1).

As the Wnt pathway is involved in cancer cell maintenance,[42] we examined whether treating PDM30 with CBZ for 48 h would introduce alterations in components at the proteome level. We identified a total of 45 proteins whose expression was changed (Figure 4F), including β-catenin (encoded by the *CTNNB1* gene) and a putative subnetwork (Figures S6C and S6E) among other signaling pathways that might be

also affected by the inhibition of CYP3A5 (Figures S7A, S7B, S7C and S7D). To demonstrate the extent of interference with the Wnt signaling pathway resulting from CYP3A5 inhibition, we treated PDM30 and PDM24 with the porcupine inhibitor IWP-2,[43] alone or in combination with CBZ, for 7 days. IWP-2 alone caused a consistent size decrease in PDM30 but not in PDM24 (Figure 4G and 4H), suggesting that PDM30, in contrast to PDM24, required Wnt signaling for 3D growth. Similar results were observed with AsPC-1 vs. $3A5^{-/-}$ OLs (data not shown). Remarkably, combination treatment with IWP-2 and CBZ sensitized PDM24 to Wnt inhibition and enhanced the organoid shrinkage response in PDM30 (Figure 4G and 4H). We confirmed that CBZ inhibited cellular proliferation by measuring the levels of Ki-67 expression with HCI in PDM30. The Ki-67 index decreased after the CBZ treatment of PDM30 for 7 days and showed dosage dependency (Figure S6F). Also, we observed that CBZ caused a decrease in mitochondrial membrane potential in PDM30 organoids at very low dosages (Figure S7E), indicating a potential mitotoxicity effect. We scored our cohort of PDACO against the Wnt signaling pathway genes (GO:0016055) by examining the full lists of somatic mutations in each PDACO (Tables S3 and S4). We detected the presence of mutations across the 446 genes of the pathway (Figure S8A) and calculated their representation in the PDACO cohort (Figure S8B and S8C). Notably, PDM24 and PDM30 did not present mutations across the gene set (Figure S8), indicating that the interaction of CYP3A5 with the Wnt pathway in PDM30 may be mediated by CYP3A5 levels.

Taken together, our findings suggest that the CBZ-driven suppression of growth in PDM30, which is characterized by the sustained activity of CYP3A5 on an original $TP53^{G105R}$ background, depends on the blockade of cancer cell maintenance pathways involving mutant p53 functions and Wnt signaling. The apparent loss of cancer cell potential connected to CYP3A5 inhibition points to unexplored possibilities for therapeutic intervention in pancreatic cancer by using CBZ.

DISCUSSION

CYP3A5 embodies all of the requisites to be considered a drug target[44] for PDAC.[26,27] Since the initial description of selective chemical binders and enzymatic inhibitors such as CBZ,[27,29] a translational evaluation of the targeting of CYP3A5 biological activity in cancer models has been awaited. Here, we established an HCI-based platform for advanced pharmaco-profiling of CYP3A5 inhibition via CBZ in *ex vivo* PDAC-biomimicking tumor systems.[10,19] Patient-derived tumor organoids, such as PDACOs, have emerged as a state-of-the-art technology for drug testing[7,45] in precision oncology setups,[4,16,24] along with systematic microscopy assays for the morpho-phenotypic evaluation of drug effectiveness.[11,14,32] In accordance with this, we have shown that our HCI platform captured inter-patient heterogeneity in a cohort of PDACOs with respect to responses to a panel of model chemotherapeutics, indicating a typical disease landscape that is useful for addressing the contribution of CYP3A5 function to chemoresistance.

Our PDACO-guided assessment of CBZ sensitivity demonstrated that the direct inhibition of CYP3A5 elicits 3D growth susceptibility in PDAC, thus validating the "druggability" of this enzyme in cancer tissue-like models for the first time. Noll and colleagues[26] investigated the correlation of high CYP3A5 levels with drug resistance in patients across PDAC subtypes. Based on their results obtained using PDAC patient-derived models (primary cell lines propagated from primary xenografts), they proposed that highly expressed CYP3A5 sustains chemoresistance and that CYP3A5 activity must be inhibited to overcome both basal and acquired resistance to chemotherapeutics.[26] In our study, we stratified the PDACOs according to the levels of CYP3A5 protein expression and the patterns of response to its chemical inhibition by CBZ. Strikingly, medium-to-high levels of CYP3A5 prompted the PDACOs to undergo consistent shrinkage after CBZ exposure, which correlated with increased sensitivity to a range of chemotherapeutics, in contrast to the results in PDACOs expressing little or no CYP3A5. Our chemo–CBZ combination screen revealed *de novo* effectiveness of some chemotherapeutics in a personalized and unbiased manner, improving the outlook for combination cancer therapy and precision medicine.[46,47] Although an initial sensitivity to typical CYP3A5 substrates (i.e., erlotinib, dasatinib, or paclitaxel) was detected in monotherapy, the lack of synergistic responses, along with the blockade of CYP3A5 drug metabolism in corresponding drug–CBZ pairs, may reflect an incomplete or already saturated acquisition of secondary resistance through the induction of CYP3A5 expression in our models, as compared with the results reported previously.[26] However, our survey revealed true intersections with cisplatin in 63% of PDACOs and consequent breakdown of chemoresistance to this drug, an alkylating agent that induces DNA damage and causes apoptosis.[48] To our knowledge, CBZ has not yet been considered for cisplatin combination therapy of targeted cancers.[49] In the first-line treatment of advanced PDAC,[50] cisplatin is currently co-administered with gemcitabine.

The most prominent effect of CBZ alone or in combination with cisplatin was observed in the PDACO that harbors a missense mutation in the DNA-binding domain of the *TP53* gene,[51] leading to the expression of the pathogenic $TP53^{G105R}$ variant.[41] No such p53 mutation was captured in other PDACO collections,[4,16,26] but several cancer databases record the presence of this mutation in glioblastoma and in ovarian and lung tumors. Our proteomic CBZ sensitivity analysis revealed molecular signatures of CYP3A5 inhibition in the $TP53^{G105R}$ background, suggesting a suppressive effect on the cancer metabolic burden, encompassing pathways of cancer cell proliferation and survival.[40,42] Strikingly, these effects paralleled those of the withdrawal of the $TP53^{G105R}$ protein, indicating the existence of a web of mechanisms that may culminate in the arrest of cell proliferation in PDACOs. The restoration of the cytotoxic behavior of cisplatin during CBZ treatment suggests that CYP3A5 inhibition interferes with $p53^{mut}$-mediated functions such as acquired chemoresistance to cisplatin.[49] Although the exact mechanism of action that links CYP3A5 function to $TP53^{G105R}$ deserves further investigation, our data suggest that CYP3A5 contributes to chemoresistance by modulating $p53^{mut}$-dependent oncogenic pathways in PDAC, i.e., its effects are not limited to canonical drug metabolization. As mutant p53 is regarded as one of the most prominent undruggable targets in cancer,[51] targeting CYP3A5 might at least provide a means of overcoming the pro-oncogenic activity of $TP53^{G105R}$. The results of our PDACO-driven screening support the repurposing of CBZ, an FDA-approved antimycotic drug,[30] for chemotherapy of PDAC. It is noteworthy that the pharmacokinetics of CBZ and its safety for systemic administration have been demonstrated in a mouse model.[31] Based on our work, we propose a novel schematic of preclinical stratification of

patients with PDAC, using PDACOs as a model and CYP3A5 as an actionable drug target. The antitumor activity of CBZ might benefit subsets of patients, as suggested by data from tumor models expressing medium-to-high levels of CYP3A5 in pathogenic p53 backgrounds.

Limitations of the study

Our study provides proof-of-concept for utilizing panels of PDACO to evaluate drug effects and identify previously unknown vulnerability. Our goal was to deploy HCI-based screening in PDACO to evaluate the targetable vulnerability of CYP3A5 in an organoid-based drug screening system. Within an initial cohort of 11 PDACOs, we identified a predictable growth vulnerability associated with medium-high levels of CYP3A5 which potentially crosstalk with cancer-associated pathways such as Wnt and p53. However, to enrich the representation of PDACO expressing medium and high levels of CYP3A5 protein, to dissect the differential responses to CBZ for PDACO with similar levels of CYP3A5, and finally to capture the landscape of mutations in PDAC cancer driver genes (e.g., *KRAS*, *TP53*, *SMAD4* and *CDKN2A*) and evaluate the effects of CBZ across multiple genotypic backgrounds in concomitance with CYP3A5 levels, it will be necessary to increase the size of the PDACO cohort. Our work paves the way for future PDACO large-scale trials to interrogate whether CYP3A5 plays a role as a gene modifier in PDAC-associated pathways through a currently unknown interaction network.

STAR★METHODS

Detailed methods are provided in the online version of this paper and include the following:

- KEY RESOURCES TABLE
- RESOURCE AVAILABILITY
  - Lead contact
  - Materials availability
  - Data and code availability
- EXPERIMENTAL MODEL AND SUBJECT DETAILS
  - PDACO culture and maintenance
  - 3D-OL culture of AsPC-1 and H6c7 immortalized cell lines
- METHOD DETAILS
  - Miniaturization of PDACO cultures for image-based assay
  - Semi-automated organoid fixation and fluorescent staining in multi-well plates
  - High-content imaging
  - Organoid segmentation and extraction of size measurements
  - Single-dose screening of chemotherapeutics
  - Organoid-based pharmaco-profiling of CBZ
  - Profiling of drug response and z-score calculation in the primary screening
  - Screening of chemo–CBZ interaction and calculation of cisplatin–CBZ synergism
  - Protein extraction from organoids and Western blot analysis
  - Quantitative proteomics
  - MS data analysis
  - Differential protein expression and pathway enrichment analysis
  - *CYP3A5* genotyping
- QUANTIFICATION AND STATISTICAL ANALYSIS

SUPPLEMENTAL INFORMATION

Supplemental information can be found online at https://doi.org/10.1016/j.isci.2024.110289.

ACKNOWLEDGMENTS

The authors thank ALSAC for support, Keith A. Laycock, PhD, ELS, for the scientific editing of the article and members of the High Throughput Bioscience Center at St. Jude Children's Research Hospital, particularly Duane G. Currier and Marlon Trotter for assistance with laboratory automation and Sergio C. Chai for valuable discussions. Research reported in this publication was supported by the National Institute of General Medical Sciences [Grant R35GM118041] (T.C.) and by the National Institute on Aging [Grant U19AG069701] (J.P.). The content is solely the responsibility of the authors and does not necessarily represent the official views of the National Institutes of Health.

AUTHOR CONTRIBUTIONS

Conceptualization, M.B.C. and T.C.; methodology: M.B.C. (HCS/HCA, drug screening), J.W. (organoid culture maintenance and Western blot) and K.Y. (mass spectrometry); data analysis and interpretation, M.B.C with inputs from K.Y. for proteomics data. J.P. supervised the design of proteomics experiments and analysis; visualization and assembly of figures, M.B.C. (illustrations generated with Adobe Illustrator and BioRender.com); article writing, M.B.C. and T.C. with the input of all authors; article review and editing, M.B.C. and T.C.

DECLARATION OF INTERESTS

The authors declare no competing interest.

Received: November 27, 2023
Revised: April 12, 2024
Accepted: June 13, 2024
Published: June 17, 2024

REFERENCES

1. Rahib, L., Wehner, M.R., Matrisian, L.M., and Nead, K.T. (2021). Estimated projection of US cancer incidence and death to 2040. JAMA Netw. Open *4*, e214708. https://doi.org/10.1001/jamanetworkopen.2021.4708.
2. Singh, R.R., and O'Reilly, E.M. (2020). New treatment strategies for metastatic pancreatic ductal adenocarcinoma. Drugs *80*, 647–669. https://doi.org/10.1007/s40265-020-01304-0.
3. Sheikh, R., Walsh, N., Clynes, M., O'Connor, R., and McDermott, R. (2010). Challenges of drug resistance in the management of pancreatic cancer. Expert Rev. Anticancer Ther. *10*, 1647–1661. https://doi.org/10.1586/era.10.148.
4. Tiriac, H., Belleau, P., Engle, D.D., Plenker, D., Deschênes, A., Somerville, T.D.D., Froeling, F.E.M., Burkhart, R.A., Denroche, R.E., Jang, G.H., et al. (2018). Organoid profiling identifies common responders to chemotherapy in pancreatic cancer. Cancer Discov. *8*, 1112–1129. https://doi.org/10.1158/2159-8290.CD-18-0349.
5. Hutchinson, L., and Kirk, R. (2011). High drug attrition rates—where are we going wrong? Nat. Rev. Clin. Oncol. *8*, 189–190. https://doi.org/10.1038/nrclinonc.2011.34.
6. Thota, R., Maitra, A., and Berlin, J.D. (2017). Preclinical rationale for the phase III trials in metastatic pancreatic cancer: Is wishful thinking clouding successful drug development for pancreatic cancer? Pancreas *46*, 143–150. https://doi.org/10.1097/MPA.0000000000000753.
7. Loewa, A., Feng, J.J., and Hedtrich, S. (2023). Human disease models in drug development. Nat. Rev. Bioeng. *1*, 1–15. https://doi.org/10.1038/s44222-023-00063-3.
8. Tuveson, D., and Clevers, H. (2019). Cancer modeling meets human organoid technology. Science *364*, 952–955. https://doi.org/10.1126/science.aaw6985.
9. Fujii, M., and Sato, T. (2021). Somatic cell-derived organoids as prototypes of human epithelial tissues and diseases. Nat. Mater. *20*, 156–169. https://doi.org/10.1038/s41563-020-0754-0.
10. Drost, J., and Clevers, H. (2018). Organoids in cancer research. Nat. Rev. Cancer *18*, 407–418. https://doi.org/10.1038/s41568-018-0007-6.
11. Herpers, B., Eppink, B., James, M.I., Cortina, C., Cañellas-Socias, A., Boj, S.F., Hernando-Momblona, X., Glodzik, D., Roovers, R.C., van de Wetering, M., et al. (2022). Functional patient-derived organoid screenings identify MCLA-158 as a therapeutic EGFR × LGR5 bispecific antibody with efficacy in epithelial tumors. Nat. Cancer *3*, 418–436. https://doi.org/10.1038/s43018-022-00359-0.
12. Walsh, A.J., Castellanos, J.A., Nagathihalli, N.S., Merchant, N.B., and Skala, M.C. (2016). Optical imaging of drug-induced metabolism changes in murine and human pancreatic cancer organoids reveals heterogeneous drug response. Pancreas *45*, 863–869. https://doi.org/10.1097/MPA.0000000000000543.
13. Seppälä, T.T., Zimmerman, J.W., Sereni, E., Plenker, D., Suri, R., Rozich, N., Blair, A., Thomas, D.L., 2nd, Teinor, J., Javed, A., et al. (2020). Patient-derived organoid pharmacotyping is a clinically tractable strategy for precision medicine in pancreatic cancer. Ann. Surg. *272*, 427–435. https://doi.org/10.1097/SLA.0000000000004200.
14. Betge, J., Rindtorff, N., Sauer, J., Rauscher, B., Dingert, C., Gaitantzi, H., Herweck, F., Srour-Mhanna, K., Miersch, T., Valentini, E., et al. (2022). The drug-induced phenotypic landscape of colorectal cancer organoids. Nat. Commun. *13*, 3135. https://doi.org/10.1038/s41467-022-30722-9.
15. Hou, S., Tiriac, H., Sridharan, B.P., Scampavia, L., Madoux, F., Seldin, J., Souza, G.R., Watson, D., Tuveson, D., and Spicer, T.P. (2018). Advanced development of primary pancreatic organoid tumor models for high-throughput phenotypic drug screening. SLAS Discov. *23*, 574–584. https://doi.org/10.1177/2472555218766842.
16. Driehuis, E., Van Hoeck, A., Moore, K., Kolders, S., Francies, H.E., Gulersonmez, M.C., Stigter, E.C.A., Burgering, B., Geurts, V., Gracanin, A., et al. (2019). Pancreatic cancer organoids recapitulate disease and allow personalized drug screening. Proc. Natl. Acad. Sci. USA *116*, 26580–26590. https://doi.org/10.1073/pnas.1911273116.
17. Marsee, A., Roos, F.J.M., Verstegen, M.M.A., HPB Organoid Consortium, Gehart, H., de Koning, E., Lemaigre, F., Forbes, S.J., Peng, W.C., Huch, M., et al. (2021). Building consensus on definition and nomenclature of hepatic, pancreatic, and biliary organoids. Cell Stem Cell *28*, 816–832. https://doi.org/10.1016/j.stem.2021.04.005.
18. Huch, M., Bonfanti, P., Boj, S.F., Sato, T., Loomans, C.J.M., Van De Wetering, M., Sojoodi, M., Li, V.S.W., Schuijers, J., Gracanin, A., et al. (2013). Unlimited in vitro expansion of adult bi-potent pancreas progenitors through the Lgr5/R-spondin axis. EMBO J. *32*, 2708–2721. https://doi.org/10.1038/emboj.2013.204.
19. Boj, S.F., Hwang, C.I., Baker, L.A., Chio, I.I.C., Engle, D.D., Corbo, V., Jager, M., Ponz-Sarvise, M., Tiriac, H., Spector, M.S., et al. (2015). Organoid models of human and mouse ductal pancreatic cancer. Cell *160*, 324–338. https://doi.org/10.1016/j.cell.2014.12.021.
20. Baker, L.A., Tiriac, H., and Tuveson, D.A. (2019). Generation and culture of human pancreatic ductal adenocarcinoma organoids from resected tumor specimens. Methods Mol. Biol. *1882*, 97–115. https://doi.org/10.1007/978-1-4939-8879-2_9.
21. Seino, T., Kawasaki, S., Shimokawa, M., Tamagawa, H., Toshimitsu, K., Fujii, M., Ohta, Y., Matano, M., Nanki, K., Kawasaki, K., et al. (2018). Human pancreatic tumor organoids reveal loss of stem cell niche factor dependence during disease progression. Cell Stem Cell *22*, 454–467.e6. https://doi.org/10.1016/j.stem.2017.12.009.
22. Georgakopoulos, N., Prior, N., Angres, B., Mastrogiovanni, G., Cagan, A., Harrison, D., Hindley, C.J., Arnes-Benito, R., Liau, S.S., Curd, A., et al. (2020). Long-term expansion, genomic stability and in vivo safety of adult human pancreas organoids. BMC Dev. Biol. *20*, 4. https://doi.org/10.1186/s12861-020-0209-5.
23. Frappart, P.O., Walter, K., Gout, J., Beutel, A.K., Morawe, M., Arnold, F., Breunig, M., Barth, T.F., Marienfeld, R., Schulte, L., et al. (2020). Pancreatic cancer-derived organoids - a disease modeling tool to predict drug response. United European Gastroenterol. J. *8*, 594–606. https://doi.org/10.1177/2050640620905183.
24. Grossman, J.E., Muthuswamy, L., Huang, L., Akshinthala, D., Perea, S., Gonzalez, R.S., Tsai, L.L., Cohen, J., Bockorny, B., Bullock, A.J., et al. (2022). Organoid sensitivity correlates with therapeutic response in patients with pancreatic cancer. Clin. Cancer Res. *28*, 708–718. https://doi.org/10.1158/1078-0432.CCR-20-4116.
25. Collisson, E.A., Sadanandam, A., Olson, P., Gibb, W.J., Truitt, M., Gu, S., Cooc, J., Weinkle, J., Kim, G.E., Jakkula, L., et al. (2011). Subtypes of pancreatic ductal adenocarcinoma and their differing responses to therapy. Nat. Med. *17*, 500–503. https://doi.org/10.1038/nm.2344.
26. Noll, E.M., Eisen, C., Stenzinger, A., Espinet, E., Muckenhuber, A., Klein, C., Vogel, V., Klaus, B., Nadler, W., Rösli, C., et al. (2016). CYP3A5 mediates basal and acquired therapy resistance in different subtypes of pancreatic ductal adenocarcinoma. Nat. Med. *22*, 278–287. https://doi.org/10.1038/nm.4038.
27. Wright, W.C., Chenge, J., Wang, J., Girvan, H.M., Yang, L., Chai, S.C., Huber, A.D., Wu, J., Oladimeji, P.O., Munro, A.W., and Chen, T. (2020). Clobetasol propionate is a heme-mediated selective inhibitor of human cytochrome P450 3A5. J. Med. Chem. *63*, 1415–1433. https://doi.org/10.1021/ACS.JMEDCHEM.9B02067.
28. Liu, Y.T., Hao, H.P., Liu, C.X., Wang, G.J., and Xie, H.G. (2007). Drugs as CYP3A probes, inducers, and inhibitors. Drug Metab. Rev. *39*, 699–721. https://doi.org/10.1080/03602530701690374.
29. Wang, J., Buchman, C.D., Seetharaman, J., Miller, D.J., Huber, A.D., Wu, J., Chai, S.C., Garcia-Maldonado, E., Wright, W.C., Chenge, J., and Chen, T. (2021). Unraveling the structural basis of selective inhibition of human cytochrome P450 3A5. J. Am. Chem. Soc. *143*, 18467–18480. https://doi.org/10.1021/jacs.1c07066.

30. Pearce, D.J., Spencer, L., Hu, J., Balkrishnan, R., Fleischer, A.B., Jr., and Feldman, S.R. (2004). Class I topical corticosteroid use by psoriasis patients in an academic practice. J. Dermatolog. Treat. *15*, 235–238. https://doi.org/10.1080/09546630410033745.
31. Najm, F.J., Madhavan, M., Zaremba, A., Shick, E., Karl, R.T., Factor, D.C., Miller, T.E., Nevin, Z.S., Kantor, C., Sargent, A., et al. (2015). Drug-based modulation of endogenous stem cells promotes functional remyelination in vivo. Nature *522*, 216–220. https://doi.org/10.1038/nature14335.
32. Mertens, S., Huismans, M.A., Verissimo, C.S., Ponsioen, B., Overmeer, R., Proost, N., van Tellingen, O., van de Ven, M., Begthel, H., Boj, S.F., et al. (2023). Drug-repurposing screen on patient-derived organoids identifies therapy-induced vulnerability in KRAS-mutant colon cancer. Cell Rep. *42*, 112324. https://doi.org/10.1016/j.celrep.2023.112324.
33. Cutrona, M.B., and Simpson, J.C. (2019). A high-throughput automated confocal microscopy platform for quantitative phenotyping of nanoparticle uptake and transport in spheroids. Small *15*, 1902033. https://doi.org/10.1002/smll.201902033.
34. National Cancer Institute Center for Cancer Genomics. Human Cancer Models Initiative (HCMI). https://ocg.cancer.gov/programs/HCMI.
35. Lee, J., Snyder, E.R., Liu, Y., Gu, X., Wang, J., Flowers, B.M., Kim, Y.J., Park, S., Szot, G.L., Hruban, R.H., et al. (2017). Reconstituting development of pancreatic intraepithelial neoplasia from primary human pancreas duct cells. Nat. Commun. *8*, 14686. https://doi.org/10.1038/ncomms14686.
36. Moore, P.S., Sipos, B., Orlandini, S., Sorio, C., Real, F.X., Lemoine, N.R., Gress, T., Bassi, C., Klöppel, G., Kalthoff, H., et al. (2001). Genetic profile of 22 pancreatic carcinoma cell lines. Analysis of K-ras, p53, p16 and DPC4/Smad4. Virchows Arch. *439*, 798–802. https://doi.org/10.1007/s004280100474.
37. Greenblatt, D.J., Zhao, Y., Venkatakrishnan, K., Duan, S.X., Harmatz, J.S., Parent, S.J., Court, M.H., and Von Moltke, L.L. (2011). Mechanism of cytochrome P450-3A inhibition by ketoconazole. J. Pharm. Pharmacol. *63*, 214–221. https://doi.org/10.1111/j.2042-7158.2010.01202.x.
38. Bai, B., Wang, X., Li, Y., Chen, P.C., Yu, K., Dey, K.K., Yarbro, J.M., Han, X., Lutz, B.M., Rao, S., et al. (2020). Deep multilayer brain proteomics identifies molecular networks in Alzheimer's disease progression. Neuron *105*, 975–991.e7. https://doi.org/10.1016/j.neuron.2019.12.015.
39. Wang, Z., Yu, K., Tan, H., Wu, Z., Cho, J.H., Han, X., Sun, H., Beach, T.G., and Peng, J. (2020). 27-plex tandem mass tag mass spectrometry for profiling brain proteome in Alzheimer's disease. Anal. Chem. *92*, 7162–7170. https://doi.org/10.1021/acs.analchem.0c00655.
40. Mantovani, F., Collavin, L., and Del Sal, G. (2019). Mutant p53 as a guardian of the cancer cell. Cell Death Differ. *26*, 199–212. https://doi.org/10.1038/s41418-018-0246-9.
41. Kato, S., Han, S.Y., Liu, W., Otsuka, K., Shibata, H., Kanamaru, R., and Ishioka, C. (2003). Understanding the function–structure and function–mutation relationships of p53 tumor suppressor protein by high-resolution missense mutation analysis. Proc. Natl. Acad. Sci. USA *100*, 8424–8429. https://doi.org/10.1073/pnas.1431692100.
42. Reya, T., and Clevers, H. (2005). Wnt signalling in stem cells and cancer. Nature *434*, 843–850. https://doi.org/10.1038/nature03319.
43. Chen, B., Dodge, M.E., Tang, W., Lu, J., Ma, Z., Fan, C.W., Wei, S., Hao, W., Kilgore, J., Williams, N.S., et al. (2009). Small molecule–mediated disruption of Wnt-dependent signaling in tissue regeneration and cancer. Nat. Chem. Biol. *5*, 100–107. https://doi.org/10.1038/nchembio.137.
44. Hughes, J.P., Rees, S., Kalindjian, S.B., and Philpott, K.L. (2011). Principles of early drug discovery. Br. J. Pharmacol. *162*, 1239–1249. https://doi.org/10.1111/J.1476-5381.2010.01127.X.
45. Moutinho, S. (2023). Researchers and regulators plan for a future without lab animals. Nat. Med. *29*, 2151–2154. https://doi.org/10.1038/s41591-023-02362-z.
46. Palmer, A.C., and Sorger, P.K. (2017). Combination cancer therapy can confer benefit via patient-to-patient variability without drug additivity or synergy. Cell *171*, 1678–1691.e13. https://doi.org/10.1016/J.CELL.2017.11.009.
47. Caldera, M., Müller, F., Kaltenbrunner, I., Licciardello, M.P., Lardeau, C.H., Kubicek, S., and Menche, J. (2019). Mapping the perturbome network of cellular perturbations. Nat. Commun. *10*, 5140. https://doi.org/10.1038/s41467-019-13058-9.
48. Siddik, Z.H. (2003). Cisplatin: mode of cytotoxic action and molecular basis of resistance. Oncogene *22*, 7265–7279. https://doi.org/10.1038/sj.onc.1206933.
49. Dasari, S., and Tchounwou, P.B. (2014). Cisplatin in cancer therapy: molecular mechanisms of action. Eur. J. Pharmacol. *740*, 364–378. https://doi.org/10.1016/j.ejphar.2014.07.025.
50. Jiang, Y., and Sohal, D.P.S. (2023). Pancreatic Adenocarcinoma Management. In Pract. *19*, 19–32. https://doi.org/10.1200/OP.22.00328.
51. Duffy, M.J., Synnott, N.C., O'Grady, S., and Crown, J. (2022). Targeting p53 for the treatment of cancer. Semin. Cancer Biol. *79*, 58–67. https://doi.org/10.1016/j.semcancer.2020.07.005.
52. Ianevski, A., Giri, A.K., and Aittokallio, T. (2022). SynergyFinder 3.0: an interactive analysis and consensus interpretation of multi-drug synergies across multiple samples. Nucleic Acids Res. *50*, W739–W743. https://doi.org/10.1093/nar/gkac382.
53. Wang, X., Li, Y., Wu, Z., Wang, H., Tan, H., and Peng, J. (2014). JUMP: a tag-based database search tool for peptide identification with high sensitivity and accuracy. Mol. Cell. Proteomics *13*, 3663–3673. https://doi.org/10.1074/mcp.O114.039586.
54. Wu, T., Hu, E., Xu, S., Chen, M., Guo, P., Dai, Z., Feng, T., Zhou, L., Tang, W., Zhan, L., et al. (2021). clusterProfiler 4.0: A universal enrichment tool for interpreting omics data. Innovation *2*, 100141. https://doi.org/10.1016/j.xinn.2021.100141.
55. Szklarczyk, D., Morris, J.H., Cook, H., Kuhn, M., Wyder, S., Simonovic, M., Santos, A., Doncheva, N.T., Roth, A., Bork, P., et al. (2017). The STRING database in 2017: quality-controlled protein–protein association networks, made broadly accessible. Nucleic Acids Res. *45*, D362–D368. https://doi.org/10.1093/nar/gkw937.
56. Clinton, J., and McWilliams-Koeppen, P. (2019). Initiation, expansion, and cryopreservation of human primary tissue-derived normal and diseased organoids in embedded three-dimensional culture. Curr. Protoc. Cell Biol. *82*, e66. https://doi.org/10.1002/cpcb.66.
57. Caicedo, J.C., Cooper, S., Heigwer, F., Warchal, S., Qiu, P., Molnar, C., Vasilevich, A.S., Barry, J.D., Bansal, H.S., Kraus, O., et al. (2017). Data-analysis strategies for image-based cell profiling. Nat. Methods *14*, 849–863. https://doi.org/10.1038/nmeth.4397.
58. Zhao, L., Au, J.L.-S., and Wientjes, M.G. (2010). Comparison of methods for evaluating drug-drug interaction. Front. Biosci. *2*, 241–249. https://doi.org/10.2741/e86.
59. Lee, G.Y., Kenny, P.A., Lee, E.H., and Bissell, M.J. (2007). Three-dimensional culture models of normal and malignant breast epithelial cells. Nat. Methods *4*, 359–365. https://doi.org/10.1038/nmeth1015.
60. Bai, B., Tan, H., Pagala, V.R., High, A.A., Ichhaporia, V.P., Hendershot, L., and Peng, J. (2017). Deep profiling of proteome and phosphoproteome by isobaric labeling, extensive liquid chromatography, and mass spectrometry. Methods Enzymol. *585*, 377–395. https://doi.org/10.1016/bs.mie.2016.10.007.
61. Wang, H., Yang, Y., Li, Y., Bai, B., Wang, X., Tan, H., Liu, T., Beach, T.G., Peng, J., and Wu, Z. (2015). Systematic optimization of long gradient chromatography mass spectrometry for deep analysis of brain proteome. J. Proteome Res. *14*, 829–838. https://doi.org/10.1021/pr500882h.
62. Peng, J., Schwartz, D., Elias, J.E., Thoreen, C.C., Cheng, D., Marsischky, G., Roelofs, J., Finley, D., and Gygi, S.P. (2003). A proteomics approach to understanding protein ubiquitination. Nat. Biotechnol. *21*, 921–926. https://doi.org/10.1038/nbt849.
63. Ritchie, M.E., Phipson, B., Wu, D., Hu, Y., Law, C.W., Shi, W., and Smyth, G.K. (2015). limma powers differential expression analyses for RNA-sequencing and microarray studies. Nucleic Acids Res. *43*, e47. https://doi.org/10.1093/nar/gkv007.

STAR★METHODS

KEY RESOURCES TABLE

REAGENT or RESOURCE	SOURCE	IDENTIFIER
Antibodies		
Rabbit monoclonal anti-Ki67, Alexa Fluor 488 (D3B5)	Cell Signaling Technology	Cat# 11882S; RRID: AB_2687824
Mouse monoclonal anti-ECadherin (HECD-1)	Thermo Fisher Scientific;[33]	Cat# 13-1700; RRID: AB_2533003
Mouse IgG Alexa Fluor 488	Thermo Fisher Scientific;[33]	Cat# A-11001; RRID: AB_253 4069
Rabbit monoclonal anti-Cytochrome P450 3A5 (EPR4396)	Abcam	Cat# ab108624; RRID: AB_10866677
Rabbit monoclonal anti-p53 (7F5)	Cell Signaling Technology	Cat# 2527; RRID: AB_10695803
Rabbit monoclonal anti-Phospho-Histone H2A.X (Ser139)(20E3)	Cell Signaling Technology	Cat# 9718; RRID: AB_2118009
Mouse monoclonal anti–β-actin (AC-15)	Sigma-Aldrich	Cat# A5441; RRID: AB_476744
Biological samples		
PDACO line PDM24	ATCC; HCMI[34]	Cat# HCM-CSHL-0073-C25
PDACO line PDM30	ATCC; HCMI[34]	Cat# HCM-CSHL-0079-C25
PDACO line PDM36	ATCC; HCMI[34]	Cat# HCM-CSHL-0089-C25
PDACO line PDM38	ATCC; HCMI[34]	Cat# HCM-CSHL-0091-C25
PDACO line PDM39	ATCC; HCMI[34]	Cat# HCM-CSHL-0092-C25
PDACO line PDM40	ATCC; HCMI[34]	Cat# HCM-CSHL-0093-C25
PDACO line PDM41	ATCC; HCMI[34]	Cat# HCM-CSHL-0094-C25
PDACO line PDM106	ATCC; HCMI[34]	Cat# HCM-BROD-0008-C25
PDACO line PDM107	ATCC; HCMI[34]	Cat# HCM-BROD-0009-C25
PDACO line PDM168	ATCC; HCMI[34]	Cat# HCM-BROD-0229-C25
PDACO line PDM179	ATCC; HCMI[34]	Cat# HCM-BROD-0232-C25
Chemicals, peptides, and recombinant proteins		
Advanced DMEM/F12	ThermoFisher Scientific	Cat# 12634028
HEPES	ThermoFisher Scientific	Cat# 15630080
GlutaMax Supplement	ThermoFisher Scientific	Cat# 35050061
B27 Supplement	ThermoFisher Scientific	Cat# 17504044
Organoid Growth Kit (A 83-01, EGF, noggin, FGF-10, gastrin, N-acetylcysteine, nicotinamide)	ATCC	Cat# ACS-7101
RhoKinase (ROCK) inhibitor Y-27632	Sigma-Aldrich	Cat# 688000
CellMatrix Basement Membrane Gel	ATCC	Cat# ACS-3035
Penicillin/Streptomycin	ThermoFisher Scientific	Cat# 15140122
TrypLE Express enzyme	ThermoFisher Scientific	Cat#12604-013
RPMI 1640 medium	ThermoFisher Scientific	Cat# 11875-093
Keratinocyte growth medium	Lonza	Cat# CC-3111
DMEM high glucose	ThermoFisher Scientific	Cat# 11965092
Fetal bovine serum	HyClone	Cat# SH30071.03
PBS (phosphate buffered saline), pH 7.4	ThermoFisher Scientific	Cat# 10010023
Paraformaldehyde Solution (EM Grade)	Electron Microscopy Sciences	Cat# 15710
Bovine serum albumin	Sigma-Aldrich	Cat# A6003
Ammonium chloride	Sigma-Aldrich	Cat# A9434
Alexa Fluor Plus 405 Phalloidin	ThermoFisher Scientific	Cat# A30104
DRAQ5 staining solution	ThermoFisher Scientific	Cat# 62251
HCS Mitochondrial Health Kit	ThermoFisher Scientific	Cat# H10295

(*Continued on next page*)

Continued

REAGENT or RESOURCE	SOURCE	IDENTIFIER
RIPA lysis and extraction buffer	ThermoFisher Scientific	Cat# 89901
Protease inhibitor	Roche	Cat# 11836153001
PhosSTOP	Roche	Cat# 4906845001
Lys-C digestive enzyme	Wako	Cat# 129-02541
Sequencing grade modified trypsin	Promega	Cat# V5111
Standard-of-care chemotherapeutic agents (Table S2)	This paper	N/A
Target drugs (Table S2)	This paper	N/A
Critical commercial assays		
TMTpro-18plex label reagent	ThermoFisher Scientific	Cat# A52045
BCA protein assay	ThermoFisher Scientific	Cat# 23227
Deposited data		
Proteomic datasets	This paper	PRIDE ID PXD031663
Experimental models: Cell lines		
AsPC-1, human pancreas adenocarcinoma ascites metastasis cell line	ATCC	Cat# CRL-1682
Cytochrome P450 3A5 KO lines in AsPC-1 background	Wright et al.[28]	N/A
H6c7, human pancreatic duct epithelial cell line	Kerafast	Cat# ECA001-FP
L Wnt-3A cell line to obtain Wnt-3A conditioned medium	ATCC	Cat# CRL-2647
HA-R-Spondin1-Fc 293T cell line to obtain RSPO1 conditioned medium	Trevigen	Cat# 3710-001-01
Software and algorithms		
Columbus Image Data Storage and Analysis System	Perkin Elmer (Revvity)	v.2.9.0
SynergyFinder 3.0	Ianevski et al.[52]	Paper
Image Studio	LI-COR Biosciences	v3.1
FiJI/ImageJ	NIH	v.1.50i
JUMP software suite	Wang et al.[53]	Paper
ClusterProfiler (V4.0)	Wu et al.[54]	Paper
Cytoscape STRING (v.3.9.1)	Szklarczyk et al.[55]	Paper
Other		
Genotype AsPC-1	Cellosaurus database; Moore et al.[36]	https://www.cellosaurus.org/CVCL_0152
Genotypic, histological, and clinical information of PDACOs	HCMI[34]	https://ocg.cancer.gov/programs/HCMI
CellVoyager CV8000 High-Content Screening System	Yokogawa	N/A
PhenoPlate 384-well, black, optically clear flat-bottom plate	Revvity	Cat# 6057300
PhenoPlate 96-well, black, optically clear flat-bottom plate	Revvity	Cat# 6055302
Echo 555 Liquid Handler	Labcyte	N/A
Echo-qualified 384-well polypropylene (PP) source microplates	Labcyte	Cat# PP-0200
384–deep well polypropylene plates	Greiner Bio-One	Cat# 784261
96-well U-bottom plates	Greiner Bio-One	Cat# 650162
MacroSpin column PROTO 300 C18	Harvard Apparatus	Cat# 74-4107
Sep-Pak C18 column	Waters	Cat# WAT054955
Acquity UPLC BEH C18 Column	Waters	Cat# 186004690
Special peptide separation column	CoAnn Technologies	Cat# HEB07503001718I-060

RESOURCE AVAILABILITY

Lead contact

Further information and requests for resources and reagents should be directed to and will be fulfilled by the lead contact, Taosheng Chen (taosheng.chen@stjude.org).

Materials availability

This study did not generate new unique reagents.

Data and code availability

- The proteomic data have been deposited at PRIDE – Proteomics Identification Database and are publicly available. The PRIDE accession number is PXD031663 which is also listed in the key resources table.
- This paper does not report original code.
- Any additional information required to reanalyze the data reported in this paper is available from the lead contact upon request.

EXPERIMENTAL MODEL AND SUBJECT DETAILS

PDACO culture and maintenance

Eleven primary PDACO lines derived from primary tumors or from metastatic sites from the Human Cancer Models Initiative (HCMI)[34] collection were obtained through the American Type Culture Collection (ATCC, see key resources table). The PDACOs were grown in culture, passaged, and cryopreserved in accordance with recommended protocols.[56] Briefly, after organoids were dissociated with TrypLE Express enzyme (Thermo Fisher Scientific, cat. no. 12604-013), organoid cells were passed through a cell strainer with 70-μm pore size and counted with an automated cell counter (Countess II; Thermo Fisher Scientific). Single cells were resuspended in fresh CellMatrix Basement Membrane Gel (ATCC, cat. no. ACS-3035) at 5×10^5 viable cells per 100 μL, and 6–10 domes/well (200 μL volume) were dispensed back into pre-warmed 6-well culture vessels. The plates were quickly inverted to facilitate dome formation and to avoid dissociated cells sinking to the bottom of the domes before polymerization was complete. Plates were immediately placed at 37°C in a cell culture incubator for 30 min. Prewarmed organoid medium (Organoid Medium 3 formulation; ATCC) was carefully added to each well (2 mL per well), and the plates were returned to the incubator. The medium was changed every 3 days, and the organoids were passaged every 14 days. The organoid medium formulation consisted of Gibco Advanced DMEM/F12 (cat. no. 12634028) supplemented with 10 mmol/L HEPES (cat. no. 15630080), 1X GlutaMAX (cat. no. 35050061), 1X B27 supplement (cat. no. 17504044), and 1X penicillin/streptomycin (cat. no. 15140122) (all from Thermo Fisher Scientific); 500 nmol/L A 83-01, 50 ng/mL EGF, 100 ng/mL noggin, 100 ng/mL FGF-10, 10 nmol/L gastrin, 1.25 mmol/L N-acetylcysteine, 10 mmol/L nicotinamide (all from the ATCC Organoid Growth Kit, cat. no. ACS-7101); 50% Wnt-3A (ATCC, cat. no CRL-2647) and 10% R-spondin (Trevigen, cat. no. 3710-001-01) conditioned medium; and 10 μmol/L ROCK Inhibitor Y-27632 (Sigma-Aldrich, cat. no. 688000). All organoid cultures were routinely tested for Mycoplasma with negative results.

3D-OL culture of AsPC-1 and H6c7 immortalized cell lines

The same PDACO growth conditions described above were applied to the AsPC-1 parental and $3A5^{-/-}$ KO lines generated previously,[27] as well as to the human pancreatic duct epithelial cell line H6c7. Initially, the three cells lines were maintained under classical 2D culture conditions. AsPC-1 cells (ATCC, cat. no. CRL-1682) were grown in RPMI 1640 medium (Thermo Fisher Scientific, cat. no. 11875-093) supplemented with 10% fetal bovine serum (HyClone, cat. no. SH30071.03), 1% GlutaMAX (Thermo Fisher Scientific, cat. no. 35050061), and 1% penicillin/streptomycin (Thermo Fisher Scientific, cat. no. 15140122). H6c7 cells (Kerafast, cat. no. ECA001-FP) were maintained in Keratinocyte Growth Medium (Lonza Bioscience, cat. no. CC-3111). Full 3D-OL cultures were established by seeding dissociated cells in MTG domes and preparing subcultures of the OLs formed in the organoid medium formulation, using the same protocol as for PDACO culture (see above). AsPC-1 cells grown in 3D culture in CellMatrix supplemented with standard cell culture medium (e.g., RPMI 1640) failed to form true 3D spheroids (see Figure S1). All cell cultures were routinely tested for mycoplasma with negative results.

METHOD DETAILS

Miniaturization of PDACO cultures for image-based assay

Matrix-embedded PDACO cultures were miniaturized by modifying a previously described protocol[33] and by establishing a matrix-embedded culture or sandwich method in 96-well plates (Revvity, cat. no. 6055302) that was then scaled down for use with 384-well plates (Revvity, cat. no. 6057300). As a first step, the wells were coated with a thin layer of matrix, using a mixture of CellMatrix (ATCC, cat. no. ACS-3035) prepared at a final concentration of 8 mg/mL. Depending on the multi-well plate format, 25 μL (for 96-well plates) or 8 μL (for 384-well plates) of matrix mixture were applied per well, using, respectively, 8-channel or 16-channel VIAFLO electronic pipettes (Integra, cat. nos. 4641, 4646, 4623, and 4624). The matrix mixture was kept at 4°C throughout, as were the multi-well plates, which were placed on a pre-chilled aluminum plate (alloy 6061, 2.3 mm thick, 30 × 15 cm; Thermo Fisher Scientific) set on ice. After dispensation of the matrix mixture, the plates were centrifuged at 900 rpm for 15 min at 4°C to ensure uniform distribution of the ECM layer and were then quickly transferred to a CO_2 incubator, where they were maintained at 37°C for 30 min to permit gelation of the matrix bed. Meanwhile, PDACO or OL cells

were prepared for drop seeding. Single cells were resuspended at 400 cells/μL in 8 mg/mL matrix, and 13 μL (containing 5200 cells) or 4 μL (containing 1600 cells) of suspension was added to the wells of 96-well plates and 384-well plates, respectively. The droplets were seeded at the center of the solid matrix bed with multichannel pipettes. Plates were manually rocked to distribute the cells evenly then returned to the incubator at 37°C for 15 min. Finally, 80 μL (for 96-well plates) or 40 μL (for 384-well plates) of pre-warmed organoid medium was added to each well with a multichannel pipette. For PDACO cultures in miniaturized format, the medium was changed every 3 days.

Semi-automated organoid fixation and fluorescent staining in multi-well plates

A pivotal feature of our HCI pipeline is the incorporation of a CellMatrix-dissolving procedure that facilitates the deposition and immobilization of organoids in a similar focal plane near the bottom of the well in a plate and that ensures optical clearance, as previously developed and demonstrated with HT-29 colon carcinoma spheroid cultures.[33] The PDACOs and OLs were fixed *in situ* in wells with 4% paraformaldehyde (PFA) prepared from a 16% aqueous solution of EM-grade PFA (Electron Microscopy Sciences, cat. No. 15710) in HEPES buffer (0.15 mol/L, pH 7.4).[33] Pre-warmed PFA solution was dispensed into 96-well plates (150 μL/well) and 384-well plates (50 μL/well). After 30 min of fixation at room temperature, the PFA solution was removed. The wells were then washed three times with phosphate-buffered saline (PBS), and the organoids immobilized in the wells after fixation were blocked and permeabilized with 0.3% Triton X-100 for 1 h at room temperature in blocking solution containing 0.5% BSA and 50 mM ammonium chloride (NH_4Cl) (Sigma-Aldrich, cat. nos. A6003 and A9434) in PBS. After three washes with PBS, the organoids were incubated with 5 U/mL Alexa Fluor Plus 405 Phalloidin and 5 μmol/L DRAQ5 (Thermo Fisher Scientific, cat. nos. A30104 and 62251) in fresh blocking solution for 2 h at room temperature. Finally, the wells were again washed three times with PBS. For Ki-67 immunostaining, a primary rabbit monoclonal antibody conjugated to Alexa Fluor 488 (Cell Signaling Technology, cat. no. 11882S; diluted 1:200) was applied overnight in blocking solution at room temperature. For all of these steps, 8-channel or 16-channel VIAFLO electronic pipettes were used at the slowest aspiration speed. Before the image acquisition, the wells were refilled with fresh PBS and the plates were sealed. For longer preservation, the wells were filled with 0.15% PFA in PBS.[33]

High-content imaging

HCI was accomplished using an automated spinning-disk microscope (Yokogawa CellVoyager CV8000). For primary screening, an imaging regimen was established that consisted of multiplexed acquisition of actin and nuclei counterstaining, using the on-the-fly maximum-intensity z-projection (MIP) acquisition mode and a 40× water immersion objective (N.A. = 1.0) with an effective image pixel resolution of 0.164 μm in the X or Y direction. A total of 4 × 16 fields of view (FOVs) stitched together in the XY direction were imaged for every well in 96-well plates, and 3 × 12 FOVs were similarly imaged for every well in 384-well plates. As the z-span was directly dependent on the size and 3D architecture of the different tumor organoids, it was established that 102.5 slices with 2-μm spacing were necessary to image organoids in full across the z-direction. To obtain on-the-fly MIPs of organoids, a minimum of five z-planes spaced at 20-μm intervals were used; this enabled the capture of information from all PDACO and OL lines simultaneously at the maximum speed possible. On-the-fly geometric and dark correction were applied. Images were post-processed for crosstalk correction to reduce the leakage of fluorescence between channels, as simultaneous multi-color imaging for 445/45–600/37 and 525/50–676/29 fluor spectra pairs were applied when applicable.

Organoid segmentation and extraction of size measurements

Dedicated scripts were created with the Columbus Image Data Storage and Analysis System v. 2.9.0 (PerkinElmer, Waltham, MA) by optimizing pipelines described previously.[33] The "Find image region" function was used to segment the individual organoids as primary objects, using the Phalloidin channel (fluor spectra 445/45 global). Removal of border objects selection was then applied, and the organoid morphology area (in μm^2) was calculated for the primary objects. The organoid morphology area was used for batch image analysis to obtain average well measurements. Nuclei were segmented from the organoid population as secondary objects with a "Find nuclei" algorithm, using the DRAQ5 channel (fluor spectra 676/29 global). The number of nuclei per individual organoid was determined. The "Calculate properties" function was used to relate the organoids to the numbers of nuclei and to sort the population in the well by their organoid rank, defined by differences in size. The organoid morphology area and the number of nuclei per organoid were obtained for all objects analyzed by supervision of segmentation during the results extraction.

Single-dose screening of chemotherapeutics

PDACO-based therapeutic profiling was conducted with an anticancer drug panel composed of 14 standard-of-care chemotherapeutic agents (Table S2). Chemotherapeutics were prepared as 10 mM stock solutions in DMSO and stored at −20°C. The exceptions were cisplatin and oxaliplatin, which were prepared from fresh powder and resuspended in 0.9 M NaCl. The concentrations of compounds to be tested were chosen based on previous studies that established effective concentration ranges in patient-derived tumor organoids for gastrointestinal cancers or other 3D models, as well as on data from our own preparatory tests (Table S2). Drug stock solutions were manually dispensed in Echo-qualified 384-well polypropylene source plates (Labcyte, cat. no. PP-0200) that were then sealed and stored at −20°C as drug source plates. To prepare the drug assay plates, the chemotherapeutics were dispensed using an Echo 555 liquid handler (Labcyte) from the source plates into 384–deep well polypropylene plates (Greiner Bio-One, cat. no. 784261). For second compound treatment and culture medium exchange during organoid treatment, drug assay plates were prepared in duplicate for each experiment. The final DMSO concentration in wells was 0.37% after backfilling, except for wells receiving cisplatin or oxaliplatin, which were handled as aqueous solutions without

DMSO. On the day of treatment, 50 μL of pre-warmed organoid medium was added to each well to resuspend the droplets of drug solution and to enable the treatments to be transferred at the designed final concentrations to the organoid assay plates. To prepare the organoid assay plates, PDACOs and OLs were dissociated into single cells and plated in 384-well plates by applying the miniaturization protocol specified above. The 3-day-old organoids were exposed to the test compounds for a total of 7 days, as a window from day 3 to day 10 was sufficient to capture the exponential growth phase for most PDACOs in our panel and, hence, to evaluate the effect of chemotherapeutics. DMSO at a concentration of 0.37% was used as a negative control for normalization purposes. The wells of the organoid assay plates were emptied and replenished with drug-containing medium at 3 days from the initial treatment. Average measurements of organoid MIP areas were used as readouts of PDACO responses to drugs in the primary screening. The Z′ factor was 0.54, calculated using the following formula: $Z' = 1 - 3 * (\sigma Pos + \sigma Neg)/(\mu Neg - \mu Pos)$, where σNeg and σPos are the standard deviation and μNeg *and* μPos are the means of the negative (DMSO) and positive (actinomycin D) controls, respectively, in two representative PDACO/OL lines. To analyze the response to the listed chemotherapeutics alone or in combination with CBZ (see below), two 384-well screening plates were prepared and assessed. PRED and IWP-2 were included as part of the targeted drugs panel.

Organoid-based pharmaco-profiling of CBZ

Clobetasol propionate was prepared as a 30 mM stock solution in DMSO and stored at −20°C. The organoid response to CBZ was assessed by primary screening and was validated across independent experiments using 96-well plates. The MIP measurements for individual organoids were extracted by supervised segmentation and analysis of image datasets from at least two independent experiments. The IC_{50} concentration of CBZ was determined by DR curve analysis in PDACO and OL cultures. Serial two-fold dilutions of CBZ were prepared to yield final concentrations ranging from 1.2 μM to 77 μM in organoid medium. The DR plates were prepared with the Echo 555 system, following the same procedure as described above but adapted to the 96-well plate format. Briefly, the DR tests were prepared in 96-well U-bottom plates (Greiner Bio-One, cat. no. 650162), and 90 μL of pre-warmed organoid medium was added to each well to resuspend the CBZ at the designed final concentration. Organoid medium samples containing the full DR range of CBZ were transferred to the PDACO assay plates. The final DMSO concentration in the wells was 0.37% after backfilling and was the same in controls for normalization purposes. The drug-treatment regimen was delivered as described previously, and individual measurements of organoid MIP areas were extracted and analyzed after supervised segmentation. The MIP values were normalized to the respective DMSO negative controls and expressed as fold changes (FCs).

Profiling of drug response and z-score calculation in the primary screening

The average measurements of organoid MIP area per well for each chemotherapeutic or target agent, such as CBZ, in the single-dose drug screening were normalized to the values for DMSO-treated organoid sets. Normalization was effectuated within each respective PDACO or OL line, generating a matrix of FC values from each plate. Those morphometric FCs were then normalized and scaled[57] by calculating weighted z-scores. To correct our dataset for the variation introduced by PDACOs with respect to the basal differences in organoid size, we determined the best transformation operation with which to balance the scales and obtain comparable standard deviations of the means. We compared the results of centering the means for the full plate, for the PDACOs (columns), and for the treatment (rows). The last option was more effective at preserving the differences established from raw FC measurements and for reporting the differences in the response to CBZ in AsPC-1 and $3A5^{-/-}$ OLs that were used as internal quality controls to assess the ability of the approach to separate and detect validated responses correctly. The z-scores were calculated using the following formula: $= (x - \mu)/\sigma$, where μ is the median and σ is the median absolute deviation of the FC values centered for each treatment of interest. All calculations were performed with these values to visualize differences in drug response between PDACOs and OLs. Cumulative response z-scores were obtained by scaling the median and median absolute deviation of FC values grouped as chemotherapeutics or PDACO sets.

Screening of chemo–CBZ interaction and calculation of cisplatin–CBZ synergism

A drug–drug interaction or combination screen was included in the primary drug screening plates, using the 14 chemotherapeutics in combination with CBZ across the PDACO and OL panels for a total of 182 unique combinations. The single-dosage concentration for each chemotherapeutic was the same as that reported for the primary drug testing in 384-well plates, whereas CBZ was applied at a 30 μM concentration. This dosage was established as being the most effective for discriminating quantitatively between CBZ-responder and CBZ-resistant PDACO and OL lines. The treatment regimen was delivered as previously described, and individual measurements of organoid MIP areas were extracted and analyzed by supervised segmentation and calculation of FC values relative to the corresponding DMSO control. Incremental vulnerability to a drug combination, as compared to the drug alone, was calculated as a fraction of the mean of the organoid MIP values for co-therapy *vs* monotherapy as $FIR = drug + CBZ/drug$. The FIR values were $\log_2$-transformed to enable discrimination of candidate synergistic drug interactions with CBZ. The cisplatin–CBZ synergism was evaluated by constructing a DR matrix in a 96-well plate. Three-fold increasing concentrations of cisplatin from 0.06 μM to 15 μM and of CBZ from 0.24 μM to 60 μM were combined to yield a 6 × 6 matrix, and each drug was used alone to generate reference curves for the individual compounds. The treatment regimen, readout processing, and FIR calculation were performed as described. The calculation and visualization of synergy scores for cisplatin–CBZ pairs was verified using SynergyFinder 3.0.[52] The combination index (CI) for CBZ and cisplatin was calculated according the formula reported previously.[58]

Protein extraction from organoids and Western blot analysis

Total protein was extracted from organoids formed in 6–10 domes (1×10^6 viable cells in 200 μL/well) in 6-well plates, in accordance with a method reported previously.[59] After the organoid culture medium was removed and the domes were washed with cold PBS, 500 μL of ice-cold PBS with 5 mM EDTA was added to the wells to reverse the polymerization of the ECM and extract intact organoids. After gentle scraping of the well bottoms, the contents were transferred to a conical tube and centrifuged at 115 × *g* for 1–2 min. After careful aspiration of the supernatant, the organoids collected at the bottom of the tube were lysed in RIPA buffer (Thermo Fisher Scientific, cat. no. 89901) containing protease inhibitors (Roche, cat. no. 11836153001). The protein concentration was measured by BCA protein assay (Thermo Fisher Scientific, cat. no. 23227). Our standard procedures for SDS-PAGE and immunoblotting were used, as described previously.[27] The following primary antibodies were used: anti-CYP3A5 (Abcam, cat. no. ab108624; 0.24 μg/mL), anti-p53 (rabbit mAb) (Cell Signaling Technology, cat. no. #2527; diluted 1:1000), anti–phospho-histone H2A.X Ser139 (rabbit mAb) (Cell Signaling Technology, cat. no. #9718; diluted 1:1000), and anti–β-actin (Sigma, cat. no. A5441; diluted 1:5000). The protein bands were visualized with an Odyssey infrared imager (LI-COR Biosciences), and band intensity was analyzed with Image Studio Version 3.1 and FiJI/ImageJ (v.1.50i).

Quantitative proteomics

To obtain the minimum amount (20 μg) of protein required for each condition to be examined, organoids were seeded in 6-well plates and organoid pellets were obtained as described above. Samples for each time point analyzed (t0, 1 h, 3 h, 9 h, 48 h and 7 days) were prepared from duplicate plates. Samples for mass spectrometry analysis were prepared according to our optimized protocol.[60] To extract proteins, the organoid pellets were lysed in 200 μL of lysis buffer (8 M urea, 50 mM HEPES, pH 8.5, 0.5% sodium deoxycholate, and 1× phosphatase inhibitor cocktail PhosSTOP [Roche, cat. no. 4906845001]) at 4°C in a bullet blender for five cycles with 30-s intervals. Protein concentration was measured by BCA protein assay. Lysates containing 50 μg of protein were sequentially digested with Lys-C (Wako, cat. no. 129-02541; 1:100 w/w) with the addition of 1 mM DTT at 21°C for 3 h. The resulting material was diluted 1:4 with 50 mM HEPES (pH 8.5) containing 1 mM DTT and further digested with trypsin (Promega, cat. no. V5111; 1:50 w/w) overnight at 21°C. The peptides were acidified with 1% trifluoroacetic acid and desalted on a C18 spin column (Harvard Apparatus, cat. no. 74-4107). The desalted peptides were dried with a SpeedVac, resuspended in 50 mM HEPES (pH 8.5), and labeled with 18-plex TMTpro-18plex reagent (Thermo Fisher Scientific, cat. no. A52045). Complete labeling was followed by desalting on a Sep-Pak C18 column (Waters, cat. no. WAT054955). The TMT-labeled samples were fractionated by offline basic pH reverse-phase liquid chromatography. Approximately 200 μg of TMT-labeled peptides was loaded onto an Acquity UPLC BEH C18 column (Waters, cat. no. 186004690; 3.0 mm × 15 cm, 1.7-μm particle size). Injected peptides were separated on a 2-h 10%–45% gradient (buffer A: 10 mM ammonium formate, pH 8.0; buffer B: 95% acetonitrile, 10 mM ammonium formate, pH 8.0) to yield a total of 48 concatenated fractions. All fractions were stored at −80°C until analyzed by liquid chromatography with tandem mass spectrometry (LC-MS/MS). For LC-MS/MS analysis, approximately 200 ng of peptides was loaded onto a reverse-phase column (CoAnn Technology, cat. no. HEB07503001718I-060; 75 μm × 25 cm, 1.7-μm C18 resin) interfaced with a Q Exactive HF Orbitrap mass spectrometer (Thermo Fisher Scientific, cat. no. IQLAAEGAAPFALGMBFZ).[61] Peptides were eluted on a 1-h 10%–35% gradient (buffer A: 0.2% formic acid, 3% DMSO; buffer B: buffer A plus 67% acetonitrile). The mass spectrometer was operated in data-dependent mode with the following MS1 settings: resolving power of 60,000, AGC target value of 1×10^6, and maximum ion injection time of 50 ms. For the top 20 MS2 high-resolution scans, the settings were isolation window of 1.0 m/z with offset of 0.2 m/z, resolving power of 60×10^3, maximum ion injection time of 110 ms, AGC target value of 1×10^5, HCD, normalized collision energy of 32%, and dynamic exclusion duration of 10 s.

MS data analysis

Acquired MS raw data were processed using the JUMP software suite[53] to improve sensitivity and specificity. This combines the advantages of pattern matching with *de novo* sequencing tags to score putative peptide–spectrum matches (PSMs). Raw data were searched against the UniProt Human database (downloaded in April 2020). Database search parameters included precursor and product ion mass tolerance of 15 ppm, fully tryptic restriction, a maximum of two missed cleavages, static mass shift for TMT tags (+304.20714) and cysteine alkylation (+57.02146), dynamic mass shift for oxidation (+15.99491 on Met), and a maximum of three dynamic modification sites. The false discovery rate (FDR) was estimated by the target-decoy strategy.[62] The resulting PSMs were filtered by a minimum peptide length of seven residues and a mass accuracy of approximately 3 ppm. They were then grouped by precursor ion charge state, after which the cutoffs for JUMP-based matching scores were applied to reduce the FDR to approximately 1% for the proteins. To minimize redundancy, protein identifications from shared peptide sequences were grouped into unique proteins according to the principle of parsimony.

Differential protein expression and pathway enrichment analysis

The TMT intensities of proteomes (TMT channels) were grouped according to treatment, PDACO, and treatment time and were $\log_2$-transformed to calculate the fold change ($\log_2$FC), *P* value, and BH FDR (adjust *P* value) by using the limma package of R.[63] Functional enrichment analysis of gene ontology (GO) and KEGG pathways was performed with the R packages ClusterProfiler (V4.0)[54] and/or Cytoscape v.3.9.1 STRING.[55] The p53 node was introduced manually for *in silico* prediction of the interaction subnetwork with differentially expressed proteins. Enrichment map and network analysis was performed with Cytoscape v.3.9.1 STRING.

CYP3A5 genotyping

Genomic DNA was isolated using High Pure PCR Template Preparation Kit protocol (Roche, 11796828001). The region around the rs776746 single nucleotide polymorphism in *CYP3A5* gene (Accession number: NG_007938.1) was amplified by PCR using primers: 5′-GGAGAGTGG CATAGGAGATACCCACG-3′ and 5′-GGGCGGGACAGGATGAAGAGTACATGG-3′. Both primers were standard, desalted oligonucleotides (ThermoFisher Scientific). Two-hundred nanogram of genomic DNA were amplified in a 50 μL reaction mixture using Phusion High-Fidelity DNA polymerase (New England BioLabs, cat. no. M0532S) and including 2 μM final concentration of each primer with/without 4% DMSO. Thermal cycling condition was: 2 min at 98 °C, 35 cycles of 15 s at 98°C, 30 s at 55°C, 2 m at 72°C, and a 10 min final extension at 72°C. The amplicon was purified using QIAquick PCR Purification Kit (Qiagen, cat. no. 28106), and the PCR fragments were Sanger-sequenced by the Hartwell Center at St. Jude Children's Research Hospital with the following primers: 5′-GAGATACCCACGTATGTACCAC-3′ and 5′-GATGCTTACCCTTCGATTTGT-3′.

QUANTIFICATION AND STATISTICAL ANALYSIS

For each experiment, sample size, number of replicates and associated statistical data analyses are indicated in the result section or figure legends. For comparison between more than two sample groups ordinary one-way ANOVA with Tukey's multiple comparisons test was used unless otherwise indicated. For comparison between two sample groups, statistical analysis was performed using the Mann–Whitney U test. Dose–response, regression, and correlation analysis, as well as the above-mentioned statistical tests were performed with GraphPad Prism (v.9.3.1). All other data were analyzed with dedicated software packages, as indicated in the STAR Methods section. All graphs were generated using GraphPad Prism (v.9.3.1) unless otherwise indicated.